Characteristics and modelling of wake for aligned multiple turbines based on numerical simulation

Runze Zhang, Zhiqiang Xin, Guoqing Huang, Bowen Yan, Xuhong Zhou, Xiaowei Deng

Characteristics and modelling of wake for aligned multiple turbines based on numerical simulation

Runze Zhang [a,b,c,d], Zhiqiang Xin [e], Guoqing Huang [b,*], Bowen Yan [b], Xuhong Zhou [b], Xiaowei Deng [f]

[a] Energy Research Institute, Qilu University of Technology (Shandong Academy of Sciences), Jinan, Shandong, 250014, China
[b] School of Civil Engineering, Chongqing University, Chongqing, 400045, China
[c] Yangjiang Offshore Wind Energy Laboratory, Yangjiang, Guangdong, 529500, China
[d] LMEE Univ-Evry, Université Paris-Saclay, 91020, Evry, France
[e] The College of Mechanics and Materials, Hohai University, Nanjing, 210098, China
[f] Department of Civil Engineering, The University of Hong Kong, 999077, Hong Kong, China

Wind energy has become one of the most commercially prospective renewable energies. However, the wake effect of wind turbine can reduce the power generation efficiency and increase the fatigue loading of downstream turbines. Hence, the wake effect study has attracted increasing interests. Compared with the extensive study on the single turbine wake, that on the superposition effect of multiple turbine (multi-turbine) wakes is limited. In this study, the characteristics of the wake velocity and turbulence intensity are studied and the exponential superposition model is proposed for the aligned multi-turbine wakes. Firstly, Simulator for Offshore Wind Farm Applications (SOWFA), a high-fidelity simulator for the interaction between wind turbine dynamics and the flow in a wind farm, is used to analyze the distribution of aligned multi-turbine wakes. It is observed that wakes reach the steady state from second turbine in the aligned turbines. Then influences of different factors on the accuracy of existing superposition models are studied. It is found spacing has significant effect on the performance of superposition models. Furthermore, the exponential superposition model with higher applicability is proposed for the wake velocity and turbulence intensity. Finally, this model is validated by the benchmark data of real wind farms.

1. Introduction

With the development of the global economy, the energy shortage and environmental pollution have become more and more serious (Sawyer et al., 2018). The rapid development of renewable energies, such as wind energy, has gradually become an important way to solve these problems (Sanderse, 2009). Study shows that the wake effect of the wind turbine can lead to a power loss up to 10–20% in a wind farm under nominal operating conditions (Barthelmie et al., 2009). Also, the additional turbulence induced by the wake will cause the larger vibration and fatigue damage to the downstream turbines (Thomsen and Sørensen, 1999). Therefore, the investigation on the wake effect of the turbine is important if the owner wants to enhance the power generation efficiency and elongate the service life of downstream turbines, especially for the offshore wind farm where the ambient turbulence intensity is relatively smaller and the wake recovers more slowly (Ishihara et al., 2004).

The investigation of the turbine wake can be carried out by field measurement, wind tunnel experiment and numerical simulation. Although field measurement reflects the wake in real world, its accuracy may be significantly affected by the factors such as the unstable wind field and harsh monitoring environment. Also, its cost is very high. Hence, it is rarely used. Compared with the field measurement, the wind tunnel experiment can control the inflow more conveniently and is widely used (Espana et al., 2012). Although the wind tunnel experiment can provide an effective and reliable way to predict the wind turbine wake, miniature turbine models have to be used due to the limited size of the wind tunnel, which leads to a large difference in the Reynolds numbers between the prototype turbine and turbine model. This Reynolds number difference may affect the scaling of experimental results

* Corresponding author.
E-mail address: ghuang1001@gmail.com (G. Huang).

from the model scale to the full scale (Tang et al., 2019). With the development of computer technology and the improvement of the accuracy of the numerical simulation, the numerical simulation will be more cost-effective than the field measurement and wind tunnel experiment. It can simulate the full-scale turbines to avoid the Reynolds number effect, and is easier to visualize and analyze the three-dimensional wake structure (Mo et al., 2013a) (Mo et al., 2013b). At present, numerical simulation has become one of the most popular methods to study turbine-wake interaction (Ti et al., 2020) (Mehta et al., 2014).

If the solid model is adopted to characterize the turbines in the simulation, the efficiency is low due to the high demand on the huge computational resource (Sørensen, 2009). On the other hand, the actuator method based on the blade element momentum theory has the advantages of smaller mesh size, higher computational efficiency and satisfactory accuracy (Martínez-Tossas et al., 2015a), which has been widely used. In the actuator disk method (ADM), the turbine is modeled as distributed forces (including axial force and tangential force) acting on the rotor disc (Martínez-Tossas et al., 2015a) (Porté-Agel et al., 2010). Wu and Porté-Agel (2011) compared ADM considering rotation to ADM without considering rotation (excluding the turbine tangential force), and it was shown that ADM with rotation performed better in the near-wake region. In the actuator line method (ALM), the lift and drag of blades is distributed on the line from the hub to the blade tip to simulate the blade rotation effect (Martínez-Tossas et al., 2015a). Sørensen and Shen (Sorensen and Shen, 2002) used ALM to predict the power of a Nordtank turbine with a rated power of 500 kW and obtained pretty good results. Draper et al. (2018) used a large eddy simulation (LES)-actuator line method framework to simulate single turbine wake and multi-turbine wakes in order to make a comparison with the wind tunnel experiments, and a good agreement between them was obtained for wake characteristics and the power coefficient. Churchfield et al. (2012a) used the open source software Simulator fOr Wind Farm Applications (SOWFA) developed by the National Renewable Energy Laboratory (NREL) in the United States to investigate the influence of atmospheric stability and roughness height on the dynamic characteristics of the turbine by coupling LES and ALM with the Fatigue, Aerodynamics, Structures, and Turbulence (FAST) turbine system and structural dynamics model (Jonkman and Buhl, 2005).

By comparing ALM with ADM, Martinez et al. (2012) found that the relative error of ALM was less than 4%, while the error of ADM was 8% at least. Breton et al. (2017) and Martínez-Tossas et al. (Martínez-Tossas et al., 2015b) indicated that ADM was unable to produce the blade tip and root vortex compared to ALM, although these two methods can generate almost same wake velocity profiles in the far wake region. Kalvig et al. (2014) compared the wake velocity profiles of the wind tunnel experiment with those of ALM and ADM, and proved that ADM had better efficiency while ALM had better accuracy. A number of scholars from different institutions were invited by Norwegian University of Science and Technology to simulate the wakes of single turbine, aligned and non-aligned 2 turbines that had been extensively tested in a wind tunnel (Krogstad and Eriksen, 2013) (Pierella et al., 2014) (Krogstad et al., 2015). They adopted various RANS turbulence models, U-RANS, and LES combined with the actuator methods to carry out numerical simulation of wake flow and found that under the condition of correct setting, LES combined with ALM could provide the most accurate wake results. Therefore, LES and ALM will be selected in this paper to simulate turbine wakes.

Although the accuracy of the numerical simulation has been widely accepted, the demand on the computational resource and time makes it difficult to be applied on the wind farm optimization and the control strategy such as the yaw control. Based on the wind tunnel experiments and numerical simulations, combined with the wind turbine aerodynamic theory, the wake models have been proposed (Bastankhah and Porté-Agel, 2014) (Niayifar and Porté-Agel, 2016) (Ishihara and Qian, 2018). Their accuracy has also been validated by the field data (Brugger et al., 2020). Jensen (1983) proposed the first wake model in 1983. He assumed that the velocity profile within the wake region was a constant, with a shape of top-hat. Katic et al. (1986a) also studied this top-hat model and believed that the main purpose of this model was to estimate the wake energy rather than accurately describe the velocity field. Since Gaussian distribution of turbine wake was observed in field tests (Gaumond et al., 2014; Nygaard et al., 2013), wind tunnel experiments (Zhang et al., 2013; Porté-Agel et al., 2011) and numerical simulations (Wu and Porté-Agel, 2012), Bastankhah and Port-Agel (Bastankhah and Porté-Agel, 2014) proposed a Gaussian wake velocity model based on the momentum conservation and mass conservation. In this model, the wake velocity deficit is expressed as the product of the amplitude function of maximum velocity deficit and Gaussian distribution function of cross section. Its wake velocity results are much more accurate than Jensen model. But the wake width growth rate, k^*, associated with the inflow turbulence intensity and thrust coefficient from the numerical simulation, is not given as a general formula, and thus limits the application of the model in practice. Based on the study of Bastankhah and Porte-Agel (Bastankhah and Porté-Agel, 2014), Niayifar and Porte-Agel (Niayifar and Porté-Agel, 2016) fitted the formula of k^* as the function of the inflow turbulence intensity. Further, Ishihara and Qian (2018) fitted the main parameters in the model, including k^*, into the formula of the inflow turbulence intensity and thrust coefficient. Also, they took a first order Taylor expansion of the amplitude function developed by Bastankhah and Porte-Agel (Bastankhah and Porté-Agel, 2014) and obtained a concise model. Kim et al. (2018) compared several widely used single wake models with wind tunnel experiments, and found that Ishihara-Qian wake model (Ishihara and Qian, 2018) is more accurate than the others. Lopes et al. (2022) adopted experimental SCADA data obtained in an onshore wind farm with eight turbines to assess five widely used analytical wake models, and Ishihara-Qian wake model (Ishihara and Qian, 2018) is one of the best two models among them.

The added turbulence intensity (defined as the additional turbulence intensity on the inflow turbulence intensity for downstream turbine) is also a very important part of the wake. Early, wake turbulence intensity models generally described the maximum added turbulence intensity $\Delta I_{\max}$ near the blade tip of the wake profile. The empirical model proposed by Quarton and Ainslie (1990) believed that $\Delta I_{\max}$ was proportional to the inflow turbulence intensity and thrust coefficient. Later, the model by Quarton and Ainslie (1990) was partially modified by Hassan and Hassan (1993). Based on the numerical simulation, Crespo and Hernandez (Crespo and Herna, 1996) proposed a wake turbulence intensity model for the induction factor with a range between 0.1 and 0.4. This model was mainly used in the far wake region. It was similar to the model of Quarton and Ainslie (1990), but the variables were changed to the induction factor and inflow turbulence intensity. The aforementioned turbulence intensity models are in a shape of top-hat. Ishihara and Qian (2018) used the double-Gaussian distribution to describe the shape of added turbulence intensity profile, and the variables were inflow turbulence intensity and thrust coefficient. Compared with the wind tunnel experiment and numerical simulation results, Ishihara and Qian's model provides more accurate prediction results.

The wake models mentioned above are suitable to calculate the wake behind a turbine. If the wake affected by multiple turbines is needed to be determined, the superposition model should be used. Currently, 4 types of superposition models (Kuo et al., 2014; Shao et al., 2019) are widely used for wake velocity superposition, including geometric sum (GS), sum of kinetic energy deficit (SKED), linear superposition (LS) (Niayifar and Porté-Agel, 2016) and sum of squares (SS) (Voutsinas et al., 1990). In the application of these models, the velocity deficit at the ith turbine should be well defined. Currently, there are two different ways to define the velocity deficit caused by the ith turbine (Zong and Porté-Agel, 2020) (Qian and Ishihara, 2021) (Porté-Agel et al., 2020), which are the mean wind velocity perceived by the ith wind turbine and

the inflow velocity of the wind farm (Lissaman, 1979) (Katic et al., 1986b). In this paper, the wind velocity used to calculate the local individual wakes is the former one instead of the latter one (Lissaman, 1979) (Katic et al., 1986b) since the superposition models used the former one (Niayifar and Porté-Agel, 2016) (Voutsinas et al., 1990) have more accurate power predictions of the wind farm, as described by Zong and Porté-Agel (2020). To evaluate the precision of the different wake velocity superposition models, Tian et al. (2017) integrated the two-dimensional Jensen model (Tian et al., 2015) into different superposition models to calculate the power loss of a wind farm in only one type of inflows in different directions. In fact, the multi-turbine wakes will be affected by the mean wind velocity and turbulence intensity of the inflow and turbine spacing. Evaluating wake models more comprehensively for multiple turbines is still needed urgently (Sun et al., 2020).

Compared to the research on the velocity superposition models, limited studies focus on the turbulence intensity superposition model. To handle this problem, approximate approaches were utilized. For example, in order to validate the accuracy of the single turbine wake model in the multi-turbine wakes, Niayifar and Porte-Agel (Niayifar and Porté-Agel, 2016) used the nearest upstream turbine wake turbulence intensity to represent the inflow turbulence intensity of downstream turbines, so the single turbine wake turbulence intensity model was still used to describe the multi-turbine wake turbulence intensity. The superposition model of wake turbulence intensity was still not given. Using two wind turbines under one inflow with average velocity of 10 m/s on hub height and turbulence intensity of 0.035 on hub height, Qian and Ishihara (2021) investigated the superposition model for wind turbines with the in-line layout and partial offset layout. They then developed a turbulence intensity superposition model based on sum of squares of velocity superposition, and they proved the accuracy of this model in the Horns Rev offshore wind farm. Therefore, a more comprehensive analysis of the characteristics of the average velocity and turbulence intensity of the wake flow of multiple turbines is conducted to develop the multi-turbine wake models in this paper.

This paper is organized as follows. In Section 2, the basic principles and methods of LES and ALM are introduced in detail. In Section 3, the accuracy of numerical simulation is verified with a numerical simulation and a wind tunnel experiment, and then the distributions of average wind velocity and turbulence intensity of aligned 4-turbine wake with different inflow mean velocities, turbulence intensity and spacing are simulated and analyzed. In Section 4, the exponential superposition models for the average wind velocity and the turbulence intensity are proposed and the accuracy and applicability of different wake velocity superposition models and turbulence intensity superposition models are examined. In Section 5, the newly developed wake superposition models are verified by the data from the actual wind farms. Finally, some observations and conclusions are provided.

2. Methodology of numerical simulation

In this section, LES and ALM will be introduced.

2.1. Large eddy simulation

2.1.1. Governing equations

In order to obtain the motion characteristics of the fluid in resolved scales (large eddy scales), the incompressible Navier-Stokes equation which is spatially filtered will be solved.

The filtered continuity equation is:

$$\frac{\partial \overline{u}_j}{\partial x_j} = 0 \tag{1}$$

where the horizontal bar represents spatial filtering, and $\overline{u}_j = u_j - u_j^{'}$ denotes filtered velocities and can be obtained by the instantaneous velocity u_j minus the sub-grid scale velocity $u_j^{'}$.

The filtered momentum equation is:

$$\begin{aligned} &\frac{\partial \overline{u}_i}{\partial t} + \frac{\partial}{\partial x_j}\left(\overline{u}_j \overline{u}_i\right) \\ &= \underbrace{-2\varepsilon_{i3k}\Omega_3 \overline{u}_k}_{\mathrm{I}} \underbrace{-\frac{\partial \widetilde{p}}{\partial x_i}}_{\mathrm{II}} \underbrace{-\frac{1}{\rho_0}\frac{\partial}{\partial x_i}p_0(x,y)}_{\mathrm{III}} \underbrace{-\frac{\partial \tau_{ij}^D}{\partial x_j}}_{\mathrm{IV}} \underbrace{+g\left(\frac{\overline{\theta}-\theta_0}{\theta_0}\right)\delta_{i3}}_{\mathrm{V}} \underbrace{+\frac{1}{\rho_0}F_i^T}_{\mathrm{VI}} \end{aligned} \tag{2}$$

The left side of the equation is the time derivative term and the convection term. The right side of the equation has 6 terms. Term I denotes the Coriolis force resulting from the rotation of the earth, where ε_{ijk} is the Ricci permutation symbol of a tensor operation, and Ω_j is the rotation rate vector and expressed as $\Omega = \omega[0, \cos(\varphi), \sin(\varphi)]$, and ω is the earth's rotation speed and equal to 7.29×10^{-5} rad/s, and φ is the latitude. Term II is the modified pressure variable gradient term normalized by the density, which is $\widetilde{p} = \overline{p}(x,y,z,t)/\rho_0 - p_0(x,y)/\rho_0 + \tau_{kk}/3 + gz$, where $\overline{p}$ and p_0 are the average pressure and static pressure, respectively, ρ_0 is the reference pressure, and g is the gravitational acceleration and equals to 9.81 m/ s^2. Term III is the gradient of the driven pressure. Term IV denotes the fluid shear stress tensor, which is $\tau_{ij}^D = \tau_{ij} - \tau_{kk}\delta_{ij}/3$ (one-third the trace of the stress tensor is lumped into the modified pressure). Term V uses the assumption of Boussinesq to consider the effect of the buoyancy, where $\overline{\theta}$ is resolved potential temperature and can be solved with Eq. (3), and θ_0 is the reference temperature and is normally 300K. Term VI is the source term which describes the blade force acting on air when the turbine rotor rotates.

The transport equation of the resolver potential temperature $\overline{\theta}$ is:

$$\frac{\partial \overline{\theta}}{\partial t} + \frac{\partial}{\partial x_j}\left(\overline{u_j}\overline{\theta}\right) = -\frac{\partial q_j}{\partial x_j} \tag{3}$$

where q_j is the flux of temperature effected by the viscous and sub-grid-scale stress.

2.1.2. Sub-grid-scale model

The viscosity mainly effects the surface of the solid wall because the turbine wake is the flow with high Reynolds number. ALM is used to simulate the turbine so it is not necessary to consider the surface of solid wall of blades, and the only solid wall is the ground surface. In this case, shear stress tensor τ_{ij}^D and flux of temperature q_j are only influenced by sub-grid-scale stress except the ground boundary in the computational domain.

Stress tensor can be expressed by a linear relationship:

$$\tau_{ij}^D = -2\nu^{\mathrm{SGS}}\overline{S}_{ij} \tag{4}$$

where ν^{SGS} is the sub-grid-scale viscosity and can be derived by Smagorinsky model (Smagorinsky, 1963):

$$\nu^{\mathrm{SGS}} = \left(C_s\Delta\right)^2\left(2\overline{S}_{ij}\overline{S}_{ij}\right)^{1/2} \tag{5}$$

and $\overline{S}_{ij}$ is the resolved scale strain rate tensor:

$$\overline{S}_{ij} = \frac{1}{2}\left(\frac{\partial \overline{u}_i}{\partial x_j} + \frac{\partial \overline{u}_j}{\partial x_i}\right) \tag{6}$$

where C_s is the model constant and set to be 0.13, $\Delta = (\Delta x \Delta y \Delta z)^{1/3}$ is the truncation scale of LES.

Flux of temperature can be expressed by a linear relationship:

$$q_j = -\frac{\nu^{\mathrm{SGS}}}{\mathrm{Pr}_t}\frac{\partial \overline{\theta}}{\partial x_j} \tag{7}$$

where Pr_t is the Prandtl number and 1/3 in neutral or unstable atmosphere, and 1 in stable atmosphere.

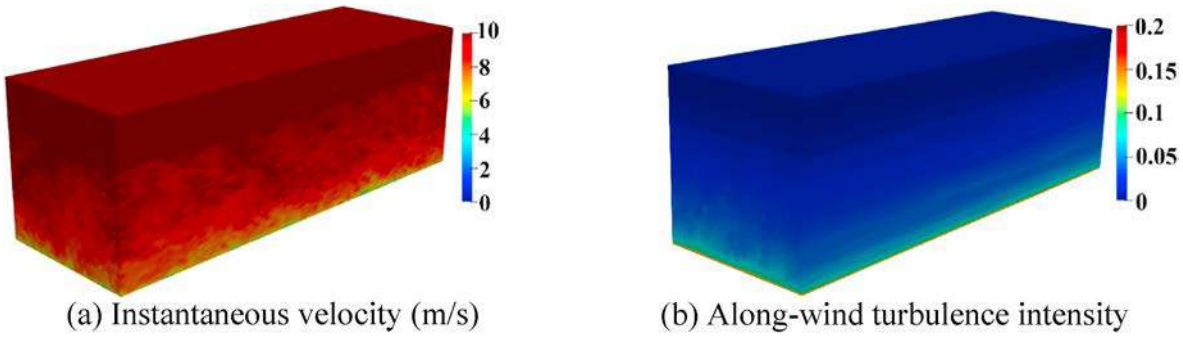

Fig. 1. Contour of simulated inflow.

2.1.3. Wall model

The computational cost of solving the flow over a solid wall increases exponentially with the increase of Reynolds number. The surface of earth is covered by rough elements, such as soil, rock and plants. So, it would require a lot of computational resources to completely solve the problem by the grid refinement. Moreover, it is not very accurate to apply non-slip boundary on the ground surface, so the wall stress model can be used to solve this problem.

The wall stress model can predict the total stress of the surface (including viscosity and sub-grid-scale stress). It is assumed that the center of the first grid cell close to the surface is located within the surface layer of the Atmospheric Boundary Layer (ABL). Accordingly, there is only the component in the vertical direction on the surface, and the rest components are all 0:

$$\tau_{ij}^{D} = \begin{bmatrix} 0 & 0 & \tau_{13}^{tot} \\ 0 & 0 & \tau_{23}^{tot} \\ \tau_{13}^{tot} & \tau_{23}^{tot} & 0 \end{bmatrix} \tag{8}$$

Schumann (1975) believed that the summation of the shear stress of the wall model is proportional to the difference between the local velocity and the horizontal average velocity at the same height:

$$\begin{aligned} \tau_{13}^{tot} &= -u_*^2 \frac{\left(\overline{u}_{1/2} - \langle \overline{u}_{1/2} \rangle\right)}{\left(\langle \overline{u}_{1/2} \rangle^2 + \langle \overline{v}_{1/2} \rangle^2\right)^{1/2}} \\ \tau_{23}^{tot} &= -u_*^2 \frac{\left(\overline{v}_{1/2} - \langle \overline{v}_{1/2} \rangle\right)}{\left(\langle \overline{u}_{1/2} \rangle^2 + \langle \overline{v}_{1/2} \rangle^2\right)^{1/2}} \end{aligned} \tag{9}$$

where 1/2 represents the center height of the grid cell at the first layer near the wall, and $\langle * \rangle$ denotes the spatial average in the horizontal direction at a specific height. The wall friction velocity is defined as:

$$u_*^2 = \left(\langle \tau_{13}^{tot} \rangle^2 + \langle \tau_{23}^{tot} \rangle^2 \right)^{1/2} \tag{10}$$

where u_* needs to be known before applying the wall model and can be approximated using the logarithmic law of the rough wall:

$$\frac{\left(\langle \overline{u}_{1/2} \rangle + \langle \overline{v}_{1/2} \rangle\right)^{1/2}}{u_*} = \frac{1}{\kappa} \ln\left(\frac{z}{z_0} + f(L) \right) \tag{11}$$

where $f(L)$ is the function related to the atmospheric stability and equal to 0 when the atmospheric stability is neutral (Etling, 1996).

2.2. Actuator line model

In actuator line model, the blade is simplified into one actuator line, and each line is discretized into a certain number of blade elements along the radial direction according to the blade element momentum theory, and then the aerodynamic force of each blade element is calculated. In addition, in order to avoid the numerical oscillation, the force at the blade element should be smoothly distributed to the surrounding mesh grid using a three-dimensional Gaussian function to obtain the volume force source term:

$$\begin{aligned} F^T &= f\eta_\varepsilon \\ \eta_\varepsilon(d) &= \frac{1}{\varepsilon^3 \pi^{3/2}} \exp\left[-\left(\frac{d}{\varepsilon} \right)^2 \right] \end{aligned} \tag{12}$$

where f is the aerodynamic force of the blade element, η_ε is Gaussian distribution adjustment function, d is the distance between the center point of the fluid grid cell and the blade element point, ε is the smoothing parameter that adjusts the blade force concentration in Gaussian distribution. The larger ε is, the smoother the distribution and the larger the influence range of volume force would be. There are several guidelines (Jha et al., 2014) for choosing the value of ε in ALM. In this paper ε is set twice the grid cell length along the actuator line as a compromise between numerical stability and accuracy recommended by Troldborg (2008).

3. Numerical simulation of turbine wake

In this paper, SOWFA developed by NREL is used to generate ABL inflow and turbine wake flow. The NREL 5 MW (Jonkman et al., 2009) wind turbine is chosen in this study. The Open Field Operations and Manipulation (Open-FOAM), 2.4.x, was used to build the solvers in SOWFA. OpenFOAM is able to solve complex partial differential equations. Finite-volume formulation is adopted to discretize the partial differential equations. Aiming to derivate at the centers of cell, this tool box interpolates the cell-centered quantities to cell faces linearly, which means second-order central differencing. Second-order backward is used for time discretization. The predictor–corrector Pressure Implicit Splitting Operation (PISO) method (Churchfield et al., 2012a) is employed as solution algorithm here in SOWFA solvers.

Firstly, the accuracy of ABL inflow and wake flow simulated in this paper is validated, and then the effects of the mean wind velocity and turbulence intensity of the inflow, and turbine spacing on the average velocity and turbulence intensity of the multi-turbine wakes are simulated and analyzed.

3.1. Validation by existing numerical simulation

3.1.1. Validation of inflow

Firstly, the simulated neutral ABL inflow in this paper is verified.

In the ABL inflow, LES solver in SOWFA is used to produce the turbulent winds in an empty domain with periodic lateral boundaries. The periodic lateral boundaries will keep the winds cycling in the flow field. When the turbulent boundary layer has reached a state that the velocity sampled at half the boundary layer height oscillates around a mean value, the data on the inflow boundary will be saved at each time step.

In the initial empty domain, the wind velocity is set to the hub-height

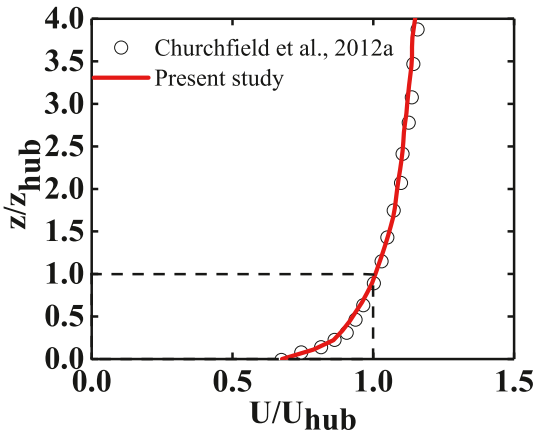

Fig. 2. Average velocity profile of simulated inflow (Churchfield et al., 2012a).

Table 1
Turbulence intensity of simulated inflow at different heights.

	I_{bot}	I_{hub}	I_{top}
Churchfield et al. (Churchfield et al., 2012a)	5.9%	4.9%	4.4%
This paper	5.6%	4.5%	4.0%
Absolute error	0.3%	0.4%	0.4%

mean wind velocity. Then small perturbations begin to act on the flow near the ground, similar to those used by de Villiers (de Villiers, 2006). From the ground surface up to 700 m, the potential temperature is 300 K. And from 700 to 800 m the potential temperature linearly increases to 308 K (capping inversion). The potential temperature increases at a rate of 0.003 K/m higher than 800 m. A fixed value is set to the pressure in the whole flow field, and it will be adjusted to maintain divergence-free flow in the first solver step. Moeng's models (Moeng, 1984) are used in SOWFA for the surface stress and temperature flux for ABL simulations. Stress and temperature flux are set to be zero at the upper boundary. Temperature and horizontal velocity are not needed to be set on the lower and upper boundaries since the stress and temperature flux have been defined at these boundaries. The velocity normal to the lower and upper boundaries is zero. For the ABL simulations, all lateral boundaries are periodic. However, in Section 3.1.2, the velocity and temperature are zero gradients on the outlet boundary.

Roughness height z_0 is 0.001 m. Hub height z_{hub} is 90 m. The mean wind velocity of the free stream in the streamwise direction U_{hub} at hub height is 8 m/s. Sub-grid-scale coefficient C_S is 0.13. The computational domain is 1000 m in the y and z directions, 3000 m in the along-wind direction, and the mesh element size is 10 m × 10 m × 10 m. The total mesh number is about 3 million in this case.

Fig. 1 shows the instantaneous wind velocity contour and turbulence intensity contour of the empty field in the computational domain. Instantaneous velocity and turbulence intensity become very stable and uniform above 750 m, which indicates that the thermal inversion layer can effectively slow down the continuous increase of the velocity above the troposphere and maintain the turbulence intensity in a low and stable state within the thermal inversion layer, and the turbulence intensity on the along-wind direction is well maintained in the whole field.

Fig. 2 shows the average velocity profile of simulations in present study and literature (Churchfield et al., 2012a). The simulated average velocity profile in this paper is satisfactorily accurate. Table 1 summarizes the inflow turbulence intensity results at different heights. In order to compare with those in literature (Churchfield et al., 2012a), the same turbulence definition $[1/3(\langle u'u'\rangle + \langle v'v'\rangle + \langle w'w'\rangle)]^{0.5}/U_{hub}$ is adopted here, where $\langle u'u'\rangle, \langle v'v'\rangle, \langle w'w'\rangle$ are Reynolds stresses in x, y, z directions, respectively, and U_{hub} is the time-averaged velocity of the free stream at hub height. I_{bot}, I_{hub} and I_{top} are the turbulent intensities at the lowest height, hub height and the highest point on the rotor disk, respectively. The maximum absolute error of the results in this paper is less than 0.4% compared with those in the literature (Churchfield et al., 2012a), which indicates that the accuracy of the inflow simulation in this paper is

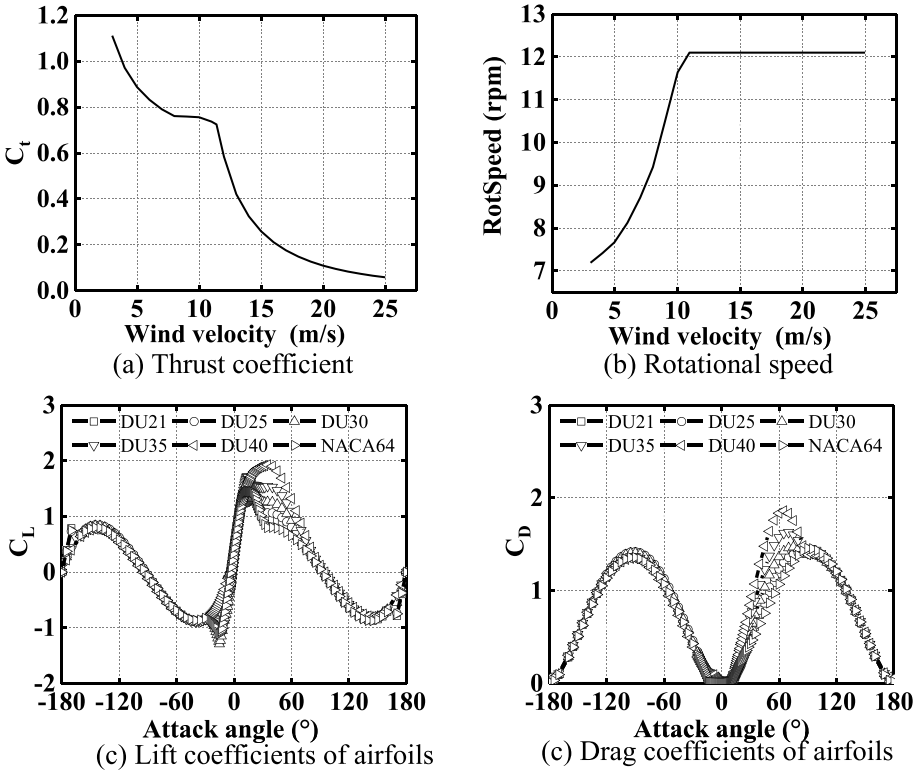

Fig. 3. Parameters of NREL 5 MW wind turbine (Jonkman et al., 2009).

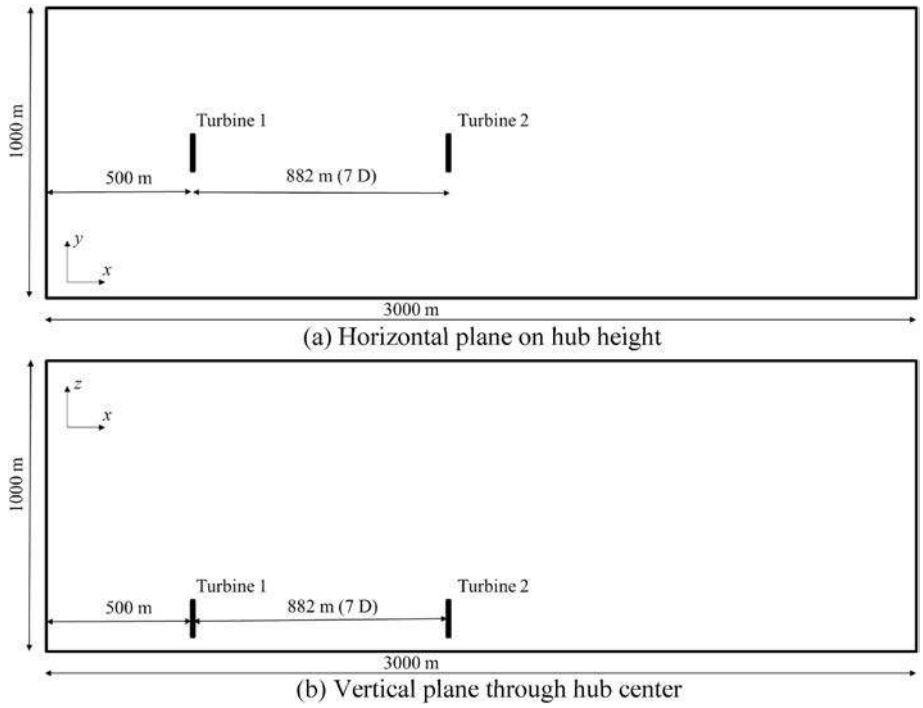

Fig. 4. The schematic of computational domain with 2 turbines.

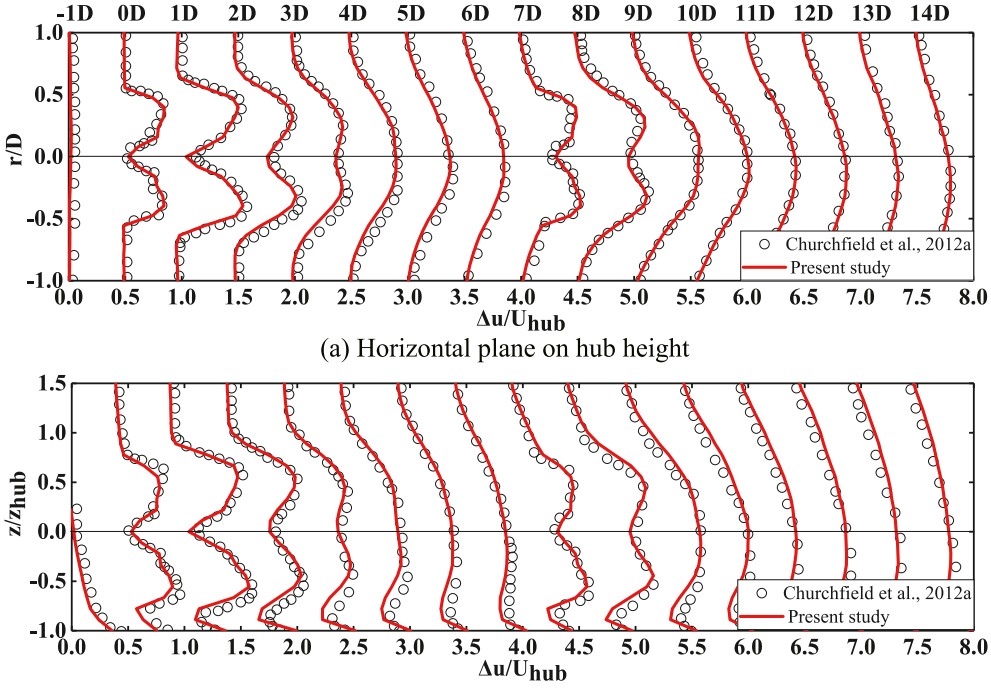

Fig. 5. Averaged deficit velocity profiles of 2-turbine wake (Churchfield et al., 2012a).

accurate enough.

3.1.2. Validation of turbine wake

Then the simulated turbine wake will be validated. Tip loss correction (Glauert, 1935) and large induced velocities correction (Glauert, 1926) are used in the wake simulation in SOWFA. Some basic parameters of NREL 5 MW wind turbine are shown in Fig. 3 (Jonkman et al., 2009). Same to settings in literature (Churchfield et al., 2012a), 2 aligned turbines are set in the inflow wind field generated in Section 3.1.1, and the spacing is 7D, where D is turbine diameter (126 m), and the computational domain is same with Section 3.1.1, as shown in Fig. 4. The local mesh is refined by 2 times in the wake region to make the mesh size to be 2.5 m × 2.5 m × 2.5 m based on the background mesh size 10 m × 10 m × 10 m. The total mesh number is about 10.7 million in this case.

Fig. 5 shows the profile of average deficit velocity $\Delta u/ U_{hub}$ of 2-

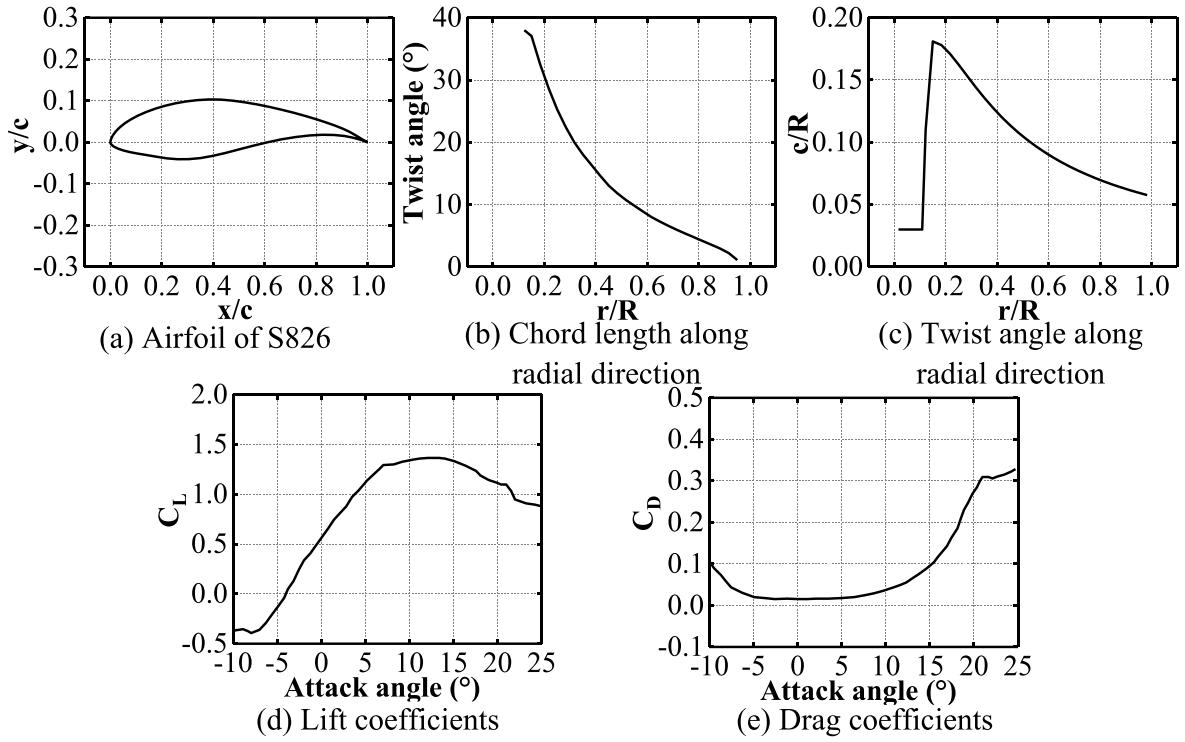

Fig. 6. Geometry and parameters of scaled wind turbine blade (Pierella et al., 2014).

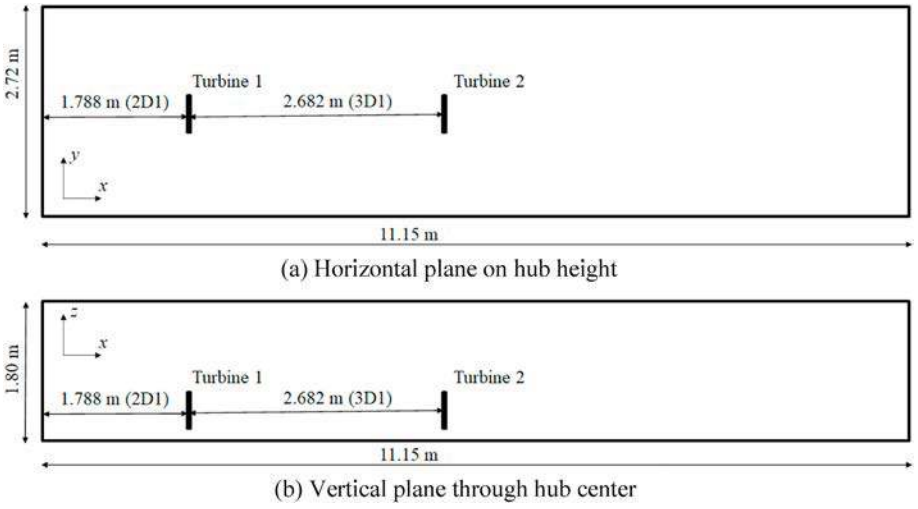

Fig. 7. The schematic of wind tunnel domain with 2 turbines.

Table 2
Comparison of thrust coefficients between numerical simulation and wind tunnel experiment (Pierella et al., 2014).

Parameter	Turbines	Wind tunnel experiment (Pierella et al., 2014)	Numerical simulation	Relative errors
C_t	Turbine 1	0.883	0.864	2.15%
	Turbine 2	0.363	0.357	1.65%

turbine wake. It can be seen that the simulation results in this paper are in good agreement with those in the literature (Churchfield et al., 2012a), and the maximum relative error of wake velocity within the rotor diameter is less than 5%. Also, wake velocity profile on the hub height plane has a shape of asymmetry, that is, if the observation direction of the turbine is defined as upstream to downstream, there will be a greater velocity deficit on the right side of the turbine. This observation has also been reported in the single turbine wake wind tunnel experiment by Pique et al. (2020) and the numerical simulation by Ishihara and Qian (2018). The turbine simulated in this paper rotates clockwise, and the direction of wake rotation is opposite to the direction of blade rotation. Therefore, the wake at a lower velocity with a lower height will be rotated to the right of the turbine, while the wake at a higher velocity with a higher height will be rotated to the left of the turbine.

The thrust coefficients of the upstream turbine and downstream turbine are 0.76 and 0.83, respectively. The inflow turbulence intensity of downstream turbine is 12%. The ratio of the power of downstream

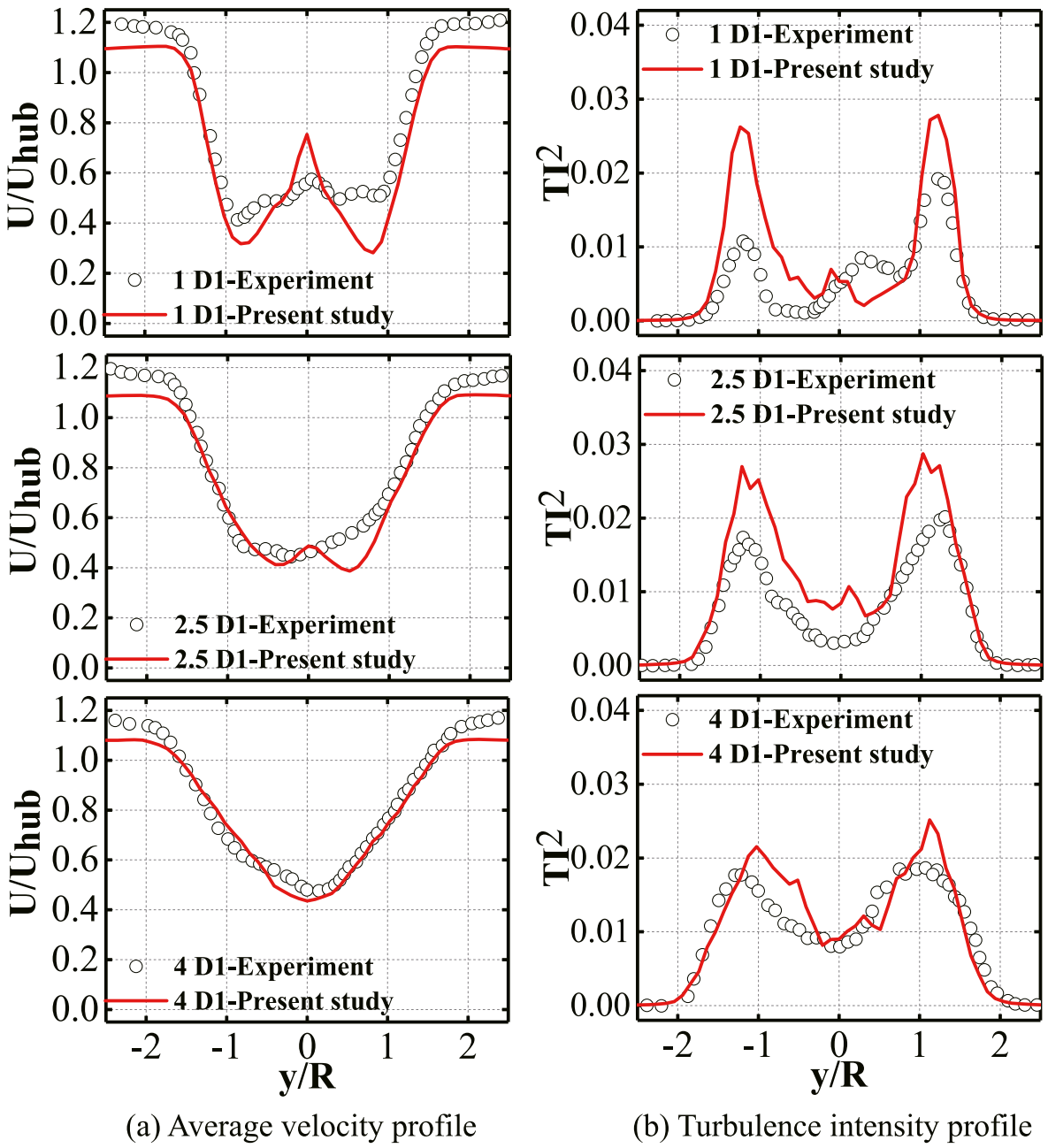

Fig. 8. Comparison of wake profiles on hub height between numerical simulation and wind tunnel experiment (Pierella et al., 2014).

Table 3
Case setting for multi-turbine wake simulation.

Case	U_{hub} (m/s)	z_0 (m)	TI (%)	Spacing (D)
1	4	0.001	5.5	6
2	7	0.001	5.5	6
3	11.4	0.001	5.5	6
4	11.4	0.02	7.5	6
5	11.4	0.2	9.5	6
6	11.4	0.001	5.5	4
7	11.4	0.001	5.5	8
8	11.4	0.001	5.5	10

turbine P_2 to that of upstream turbine P_1 can be calculated. This ratio is 0.51 and 0.56 for this study and literature (Churchfield et al., 2012a), respectively, and the difference is 8.9%. This means the accuracy of this study is sufficient.

3.2. Validation by wind tunnel experiment

The simulated turbine wake is further validated by a wind tunnel experiment (Pierella et al., 2014). The wind tunnel has a rectangular test section, with 2.72 m (width) and 1.80 m (height), and 11.15 m (length). In the experiment, the geometric and aerodynamic of the turbine blade are given in Fig. 6. Two turbines are used and their hub heights were both 0.817 m. However, their rotor sizes were slightly different, which leads to somewhat different rotor diameters: D1 = 0.894 m and D2 = 0.944 m. These two turbines were placed as shown in Fig. 7. The mean wind velocity and turbulence intensity of the free stream in the streamwise direction at hub height were 10 m/s and 0.3%. The tip speed ratios are 1200 rpm and 800 rpm for the upstream turbine and

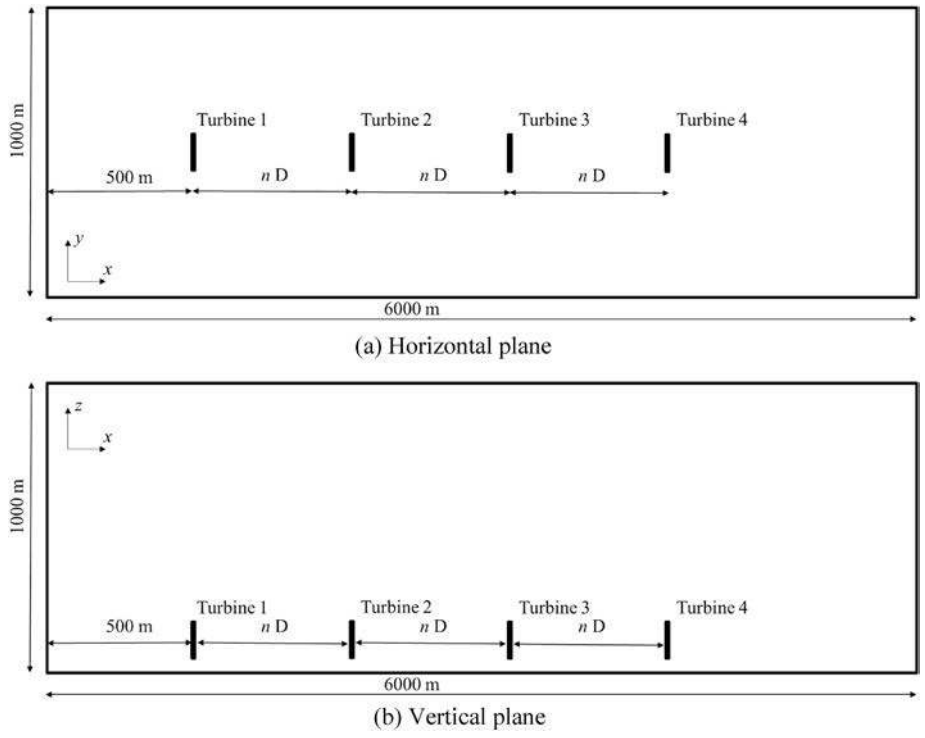

Fig. 9. The schematic of computational domain with 4 turbines.

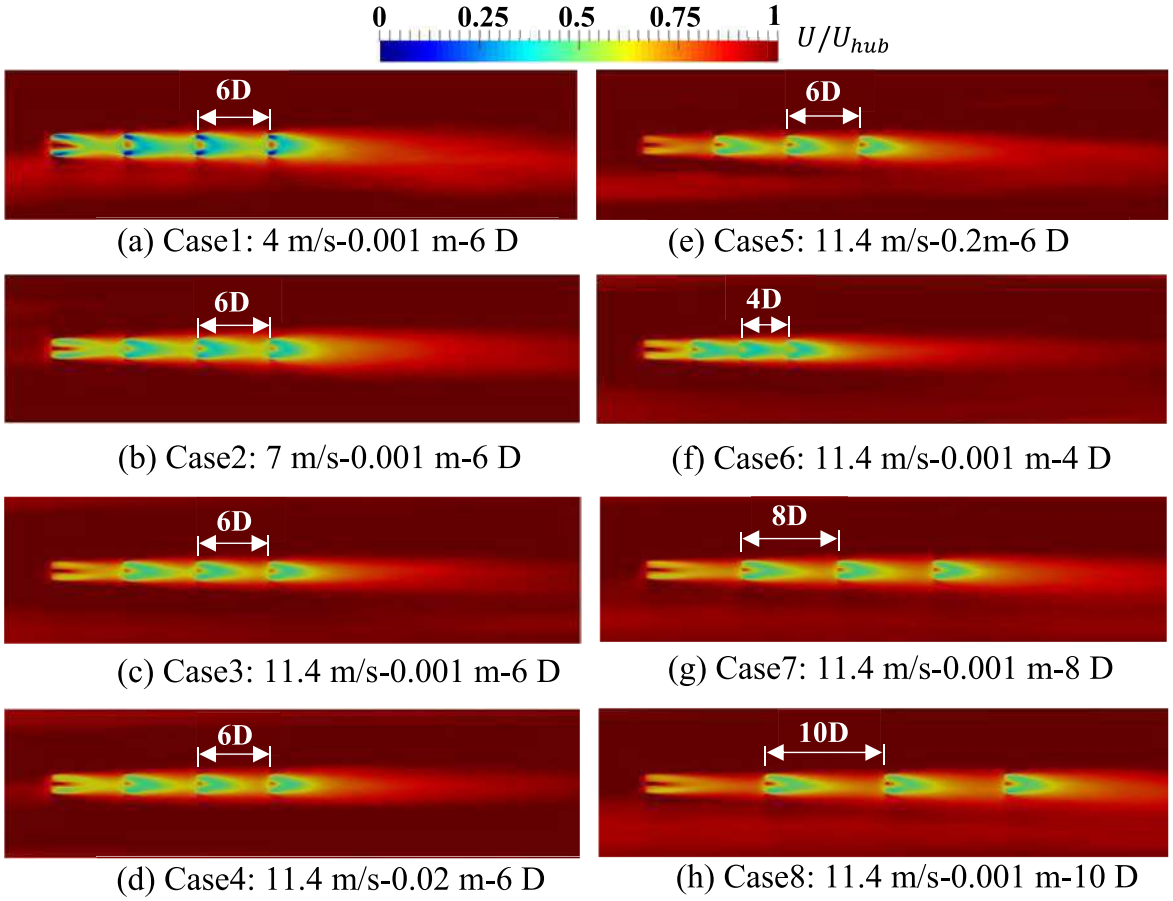

Fig. 10. Contour of wake average velocity on hub height plane.

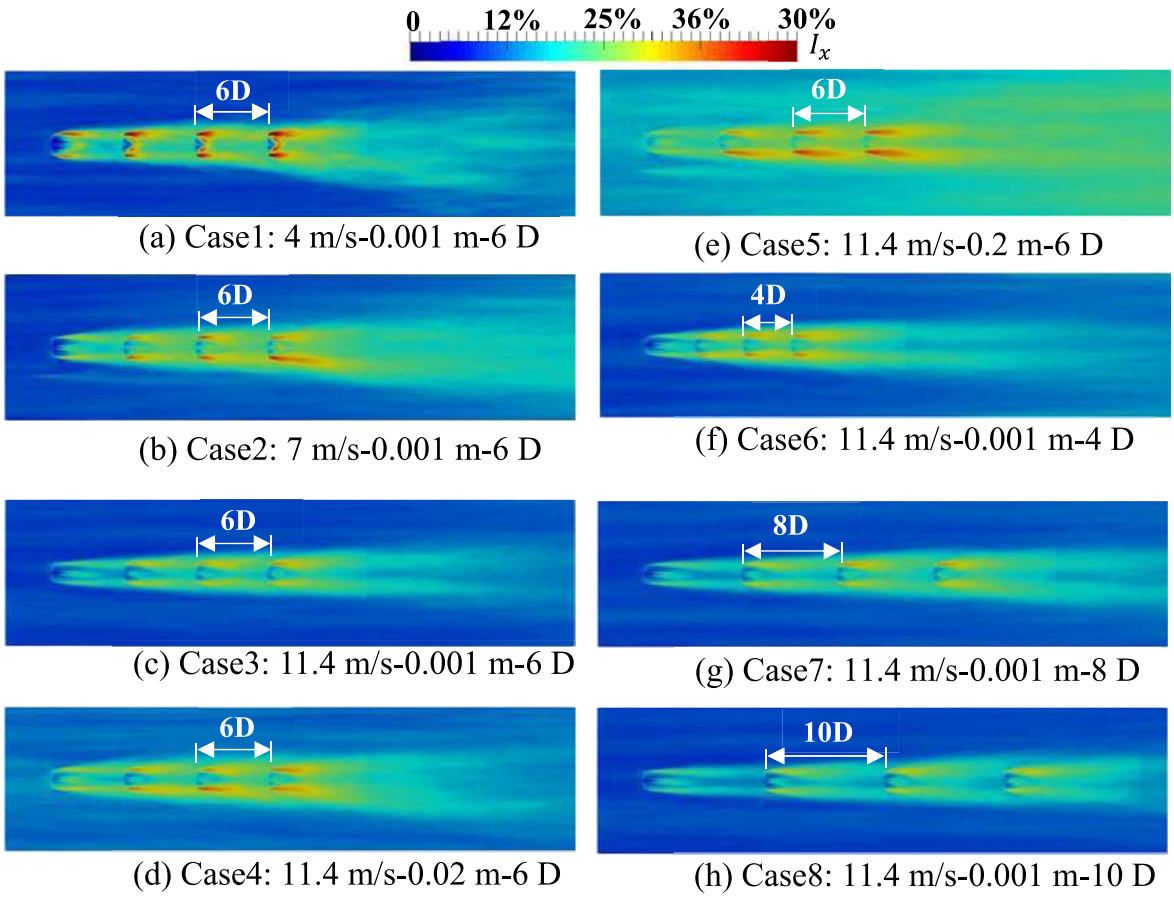

Fig. 11. Contour of wake turbulence intensity on hub height plane.

downstream turbine. In the simulation, the geometric and aerodynamic parameters of the scaled blade, the size and position of the scaled wind turbines and computation domain are same to those in the wind tunnel experiment. The local mesh is refined to make the mesh size to be 0.018 m × 0.018 m × 0.018 m. The total mesh number is about 5.3 million in this case.

Table 2 is the thrust coefficients C_t of the 2 turbines from experiment (Pierella et al., 2014) and SOWFA. Fig. 8 shows the profiles of wake velocity and turbulence intensity in along-wind direction at hub height ($TI = \sigma_x/U_{hub}$, where σ_x is the root mean squared value of along-wind instantaneous velocity). It is shown that the results of SOWFA in this paper fit well with those of the wind tunnel experiment, which proves the accuracy of the wake simulation by authors.

3.3. Numerical simulation of multi-turbine wakes

3.3.1. Case setting

Based on the aligned layout, the influence of the mean wind velocity and turbulence intensity of the inflow, and turbine spacing on the average velocity and turbulence intensity of the wake flow of multiple turbines are studied. The selection principle of relevant parameters is discussed below.

Generally, the turbine mainly works at or below the rated wind speed. Therefore, in this paper, 4 m/s (close to the cut-in wind speed), 7 m/s (between the cut wind speed and the rated wind speed) and 11.4 m/s (rated wind speed) are selected for NREL 5 MW turbine, which can reflect most working states of the turbine.

In addition to the average velocity, turbulence intensity is another important parameter. The larger the turbulence intensity is, the more intense mixing between the turbine wake and the surrounding inflow will be. Thus, the wake average velocity will recover faster. The turbulence intensity of inflow is primarily affected by the surface roughness. The higher the roughness height is, the stronger the turbulence intensity of ABL will be. According to literature (Stull, 1988), the roughness height was roughly divided into three types. In order to consider different inflow turbulence intensity, the roughness height is selected as 0.001 m (typical offshore condition), 0.02 m (flat grassland) and 0.2 m (typical onshore condition) in this paper. Hence, the inflow turbulent intensities considered in this study can cover most wind farms.

In the aligned layout, the downstream turbine is completely in the wake region of upstream turbine, which is the worst working state, so this layout is focused. Recommended distance is 3-5D between neighboring two columns (perpendicular to prevailing wind direction) and 5-9D between neighboring two rows (parallel to prevailing wind direction) (Masters, 2013). Therefore, the turbine row spacing chosen here is 4D, 6D, 8D and 10D, respectively, when the prevailing wind direction is considered.

Table 3 shows the setting of main variables in the wake simulation of multi-turbine. Cases 1–3 focus on the influence of the inflow mean velocity on the multi-turbine wake with the same setting of inflow turbulence intensity and spacing; Cases 3–5 focus on the influence of inflow turbulence intensity on the multi-turbine wake with the same setting of the inflow mean velocity and spacing; Cases 3, 6–8 focus on the influence of spacing on the multi-turbine wake with the same setting of the inflow mean velocity and turbulence intensity.

4 turbines are placed in a computational domain of 6000 m × 1000 m × 1000 m. Details are shown in Fig. 9, where the constant n depends on the spacing described in Table 3. When the wakes of 4 turbines are simulated, the local mesh is refined by 2 times in the wake region to make the mesh size to be 2.5 m × 2.5 m × 2.5 m based on the

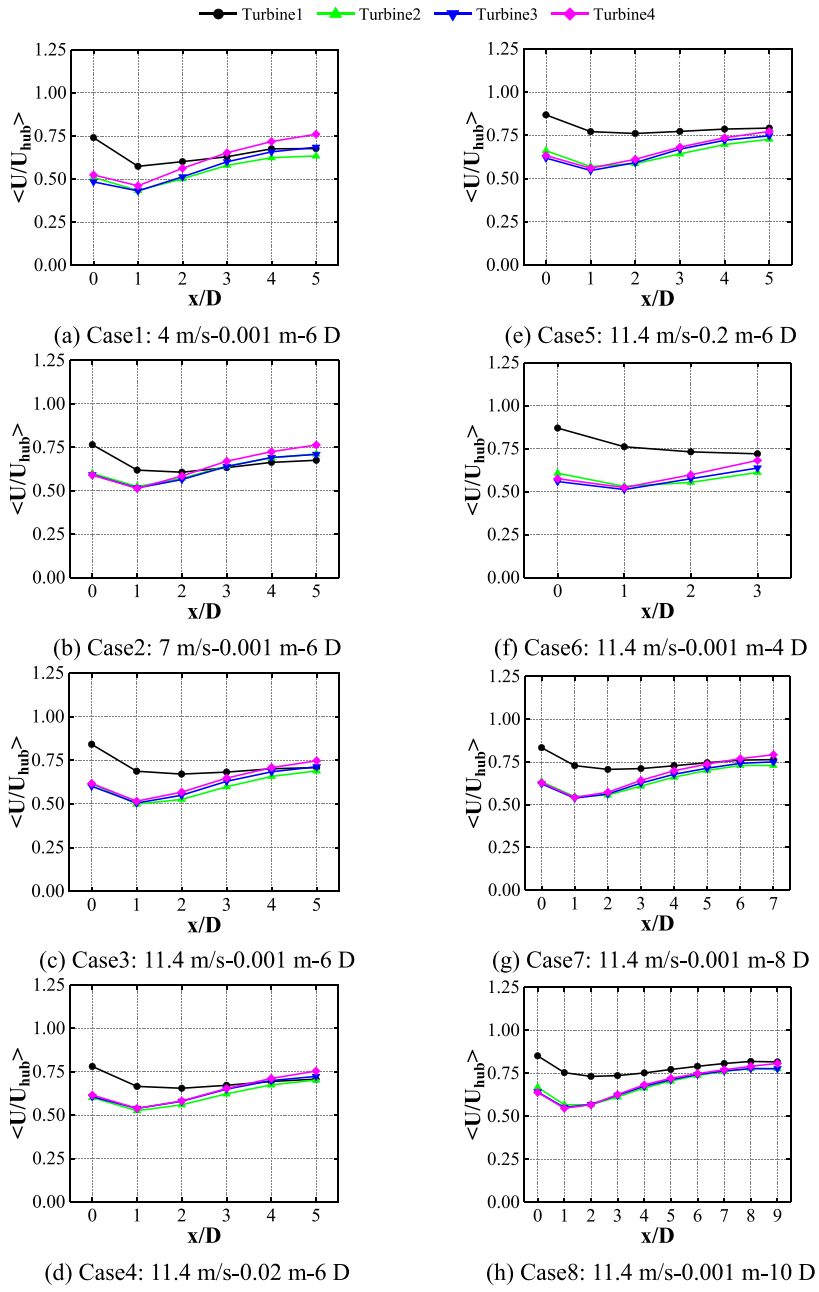

Fig. 12. Wake average velocities at different downstream positions on hub height plane.

background mesh size 10 m × 10 m × 10 m. The total mesh number is about 25 million in this case.

3.3.2. Simulation results

The numerical simulation results of multi-turbine wake are shown in Figs. 10–15. Figs. 10–11 show the contours of the average velocity and turbulence intensity on the hub height plane. Figs. 12–13 show the distribution of the average velocity and turbulence intensity which are spatially averaged within the rotor diameter on the hub height plane at different downstream locations (<*> represents spatial averaging). Figs. 14–15 show the thrust coefficients and inflow turbulent intensities of each turbine. Note that inflow turbulence intensity is determined by spatially averaging the turbulence intensity within the rotor diameter at the hub height on the plane which is located at 1 diameter ahead of the rotor.

The influence of the inflow mean velocity, turbulence intensity and spacing on turbine wake average velocity and turbulence intensity will be discussed as follows:

(1) Cases 1–3 under different inflow mean velocities. As shown in Figs. 10–11 (a)–(c) where the inflow turbulence intensity is 5.5% and the spacing is 6D, when the inflow mean velocity increases, the deficit of the average velocity of turbine wake will be smaller, and the increment of turbine wake turbulence intensity will also be smaller. This is attributed to that the thrust coefficient becomes smaller with the increase of inflow mean velocity and the corresponding influence of turbine on the air will decrease, which can be seen from Fig. 14 (a). From Figs. 12–13 (a)–(c), the following observations can be found. 1), The wake deficit of turbines 2–4 is relatively similar, which indicates that when the inflow velocity is less than or equal to the rated wind velocity, the wakes of downstream turbines will reach a steady state soon since

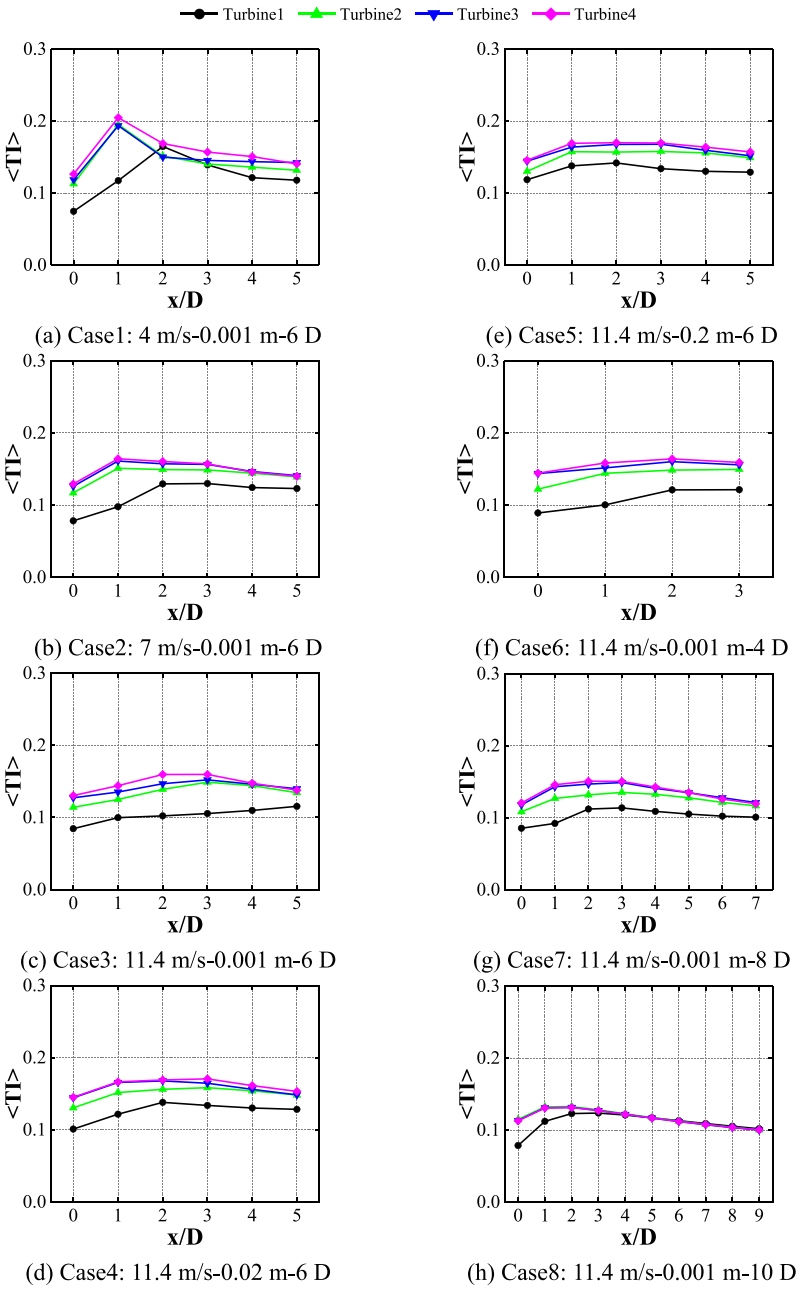

Fig. 13. Wake turbulence intensities at different downstream positions on hub height plane.

turbine 2. This phenomenon has been reported in literature (Porté-Agel et al., 2013; Churchfield et al., 2012b; Witha et al., 2014; Wu and Porté-Agel, 2015; Simisiroglou et al., 2018). 2), The wakes of turbines 2–3 recover a little bit slower than that of turbine 4. This can be explained as followings: (1) the inflow turbulence intensity of turbine 4 is higher than the inflow turbulence intensity of turbines 2–3 as shown in Fig. 15 (a); (2) the wakes of turbines 2–3 enter the high static pressure region when they propagate into far wake region, while turbine 4 is the last downstream turbine, and its wake recovers slightly faster.

(2) Cases 3–5 under different inflow turbulence intensities. As shown in Figs. 10–11 (c)–(e), where the inflow mean velocity is rated and the spacing is 6D, when the inflow turbulence intensity increases, the wake velocity of turbine 1 recovers faster, but the wake deficit of turbines 2–4 is basically the same. This is because the wake of turbine 1 is mainly affected by the inflow turbulence intensity, but turbines 2–4 are primarily affected by the wake turbulence intensity. The absolute differences of the inflow turbulence intensities of turbines 2–4 among Cases 3–5 are only around 1%, which can be seen in Fig. 15 (b). As shown in Figs. 12–13 (c)–(e), it can be seen that when the inflow turbulence intensity changes, the average velocity and turbulence intensity of the wake still remain stable since turbine 2.

(3) Cases 3, 6–8 under different spacing. As shown in Figs. 10–11 (c) and (f)-(h), where the inflow mean velocity is rated and turbulence intensity is 5.5%, when the turbine spacing increases, the wake turbulence intensity has a longer distance to recover. It can be clearly seen from the comparison of contours of wake turbulence intensity that the larger the turbine spacing is, the smaller the wake turbulence intensity of the downstream turbine will be. This could be attributed to the fact that the inflow velocity of the downstream turbine will be larger (thrust coefficient will be

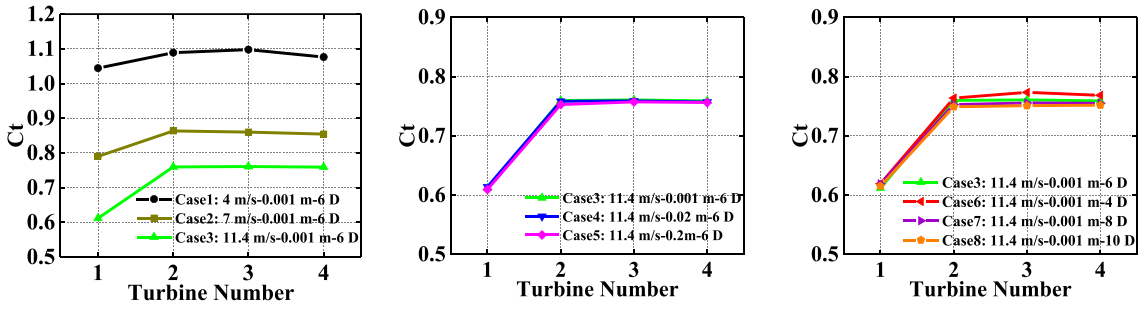

(a) Cases of different inflow mean velocities (b) Cases of different inflow turbulence intensities (c) Cases of different spacing

Fig. 14. Thrust coefficients of each turbine.

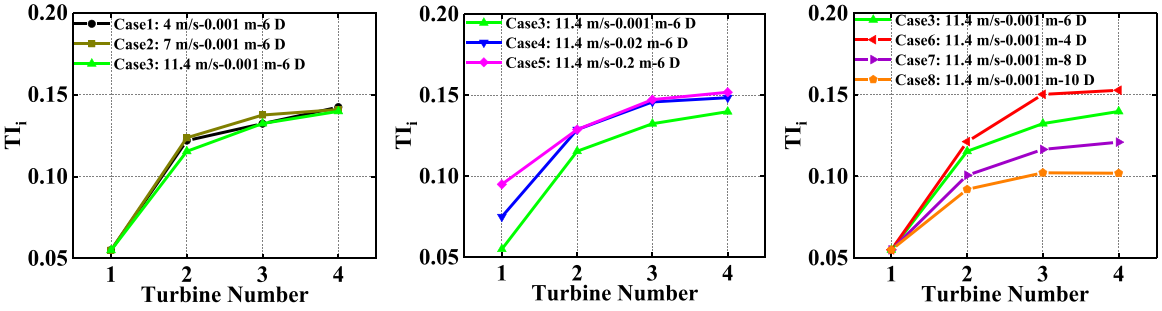

(a) Cases of different inflow mean velocities (b) Cases of different inflow turbulence intensities (c) Cases of different spacing

Fig. 15. Inflow turbulence intensities of each turbine.

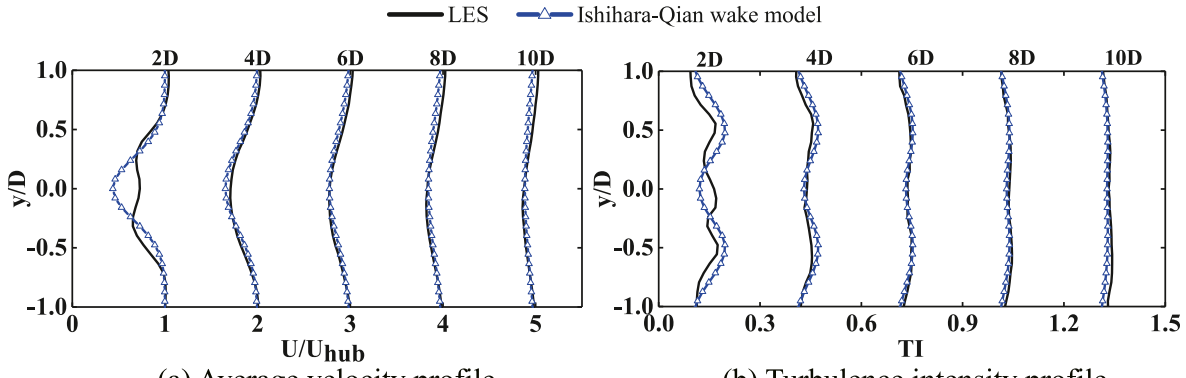

(a) Average velocity profile (b) Turbulence intensity profile

Fig. 16. Comparison of wake profiles on hub height between Ishihara-Qian wake model (Ishihara and Qian, 2018) and numerical simulation.

smaller) and the inflow turbulence intensity of the downstream turbine will be smaller. As shown in Figs. 12–13 (c) and (f)-(h), it can be seen that when the spacing changes, the average velocity and turbulence intensity of the wake are both stable since turbine 2.

4. Multi-turbine wake model

Firstly, the applicability of Ishihara-Qian wake model (Ishihara and Qian, 2018) on NREL5MW turbine is verified in section 4.1. Then the existing classic four wake velocity superposition models are summarized in section 4.2. Furthermore, the existing wake velocity superposition models will be adapted for constructing the wake turbulence intensity superposition in section 4.3. Finally, in section 4.4, the new wake superposition models will be proposed, and different models will be compared with LES simulations.

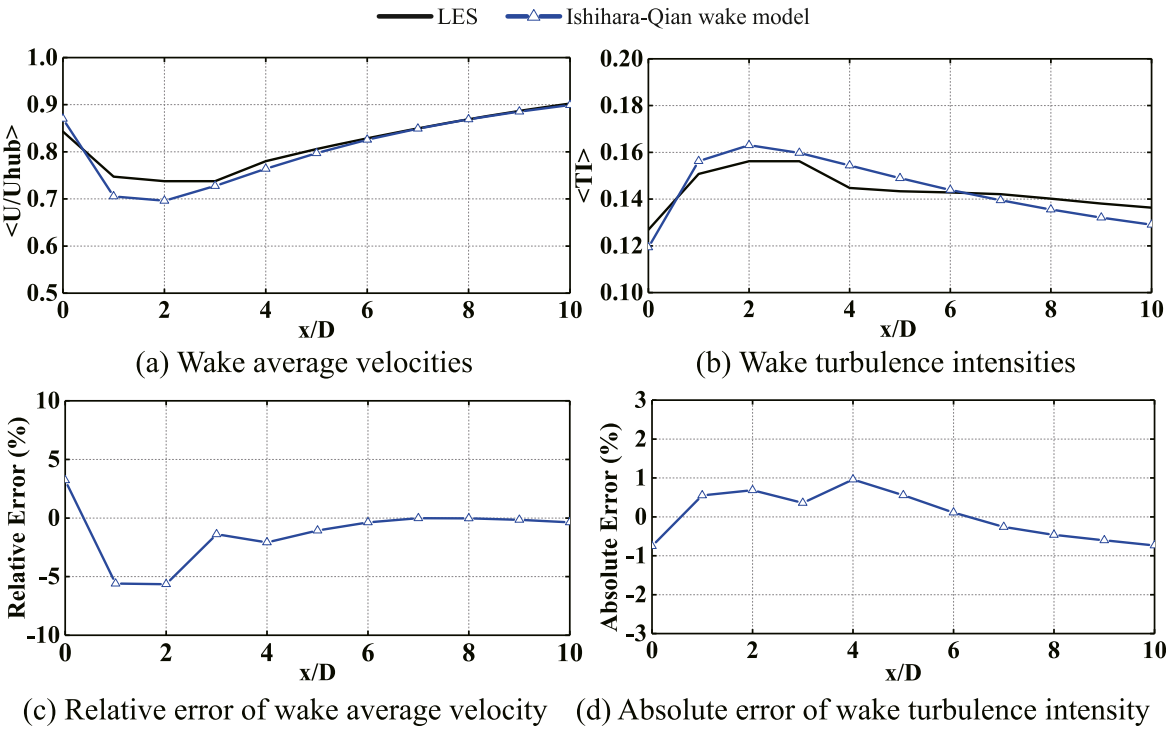

Fig. 17. Comparison of wake profiles on hub height between Ishihara-Qian wake model (Ishihara and Qian, 2018) and numerical simulation.

Table 4
Wake velocity superposition models.

Name	Formula
velocity geometric sum (V-GS)	$u_i = u_0 \prod_{j=1}^{n} \frac{u_{ij}}{u_j}$
velocity sum of kinetic energy deficit (V-SKED)	$u_i = \sqrt{u_0^2 - \sum_{j=1}^{n}(u_j^2 - u_{ij}^2)}$
velocity linear superposition (V-LS)	$u_i = u_0\left(1 - \sum_{j=1}^{n}\left(1 - \frac{u_{ij}}{u_j}\right)\right)$
velocity sum of square (V-SS)	$u_i = u_0\left(1 - \sqrt{\sum_{j=1}^{n}\left(1 - \frac{u_{ij}}{u_j}\right)^2}\right)$

Note: u_0 is the inflow velocity; u_i is the inflow velocity of turbine i; u_j is the inflow velocity of turbine j; u_{ij} is the wake velocity exerted by turbine j at the location of turbine i.

Table 5
Turbulence intensity superposition models.

Name	Formula
turbulence intensity geometric sum (TI-GS)	$I_i = I_0 \prod_{j=1}^{n} \frac{I_{ij}}{I_j}$
turbulence intensity sum of kinetic energy deficit (TI-SKED)	$I_i = \sqrt{I_0^2 + \sum_{j=1}^{n}(I_{ij}^2 - I_j^2)}$
turbulence intensity linear superposition (TI-LS)	$I_i = I_0\left(1 + \sum_{j=1}^{n}\left(\frac{I_{ij}}{I_j} - 1\right)\right)$
turbulence intensity sum of square (TI-SS)	$I_i = I_0\left(1 + \sqrt{\sum_{j=1}^{n}\left(\frac{I_{ij}}{I_j} - 1\right)^2}\right)$

Note: I_0 is the inflow turbulence intensity; I_i is the inflow turbulence intensity of turbine i; I_j is the inflow turbulence intensity of turbine j; I_{ij} is the wake turbulence intensity exerted by turbine j at the location of turbine i.

4.1. Verification of Ishihara-Qian wake model

In order to analytically determine the multi-turbine wake, the wake average velocity and turbulence intensity of single turbine should be determined first. According to the literature review in section 1, the Ishihara-Qian wake model (Ishihara and Qian, 2018) is a good candidate. However, this model is developed based on the simulation results of 2.4 MW turbine. Its applicability to NREL 5 MW turbine adopted in this paper needs to be verified. In this study, the single turbine wake of NREL 5 MW in the case of $U_{hub} = 11.4\ m/s$, $TI = 9.5\%$ and $z_0 = 0.2\ m$ is simulated. Figs. 16–17 shows the comparison between LES and Ishihara-Qian wake model. It can be seen that Ishihara-Qian wake model can provide a good prediction after 4D. Hence, this model will be adopted in the following study.

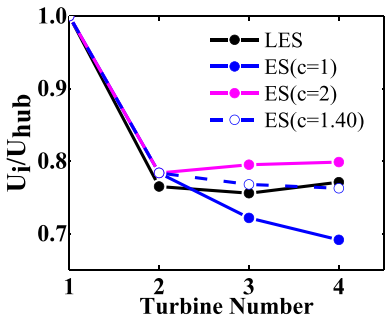

Fig. 18. Results of ES with different c in Case 3 (11.4 m/s-5.5%-6D).

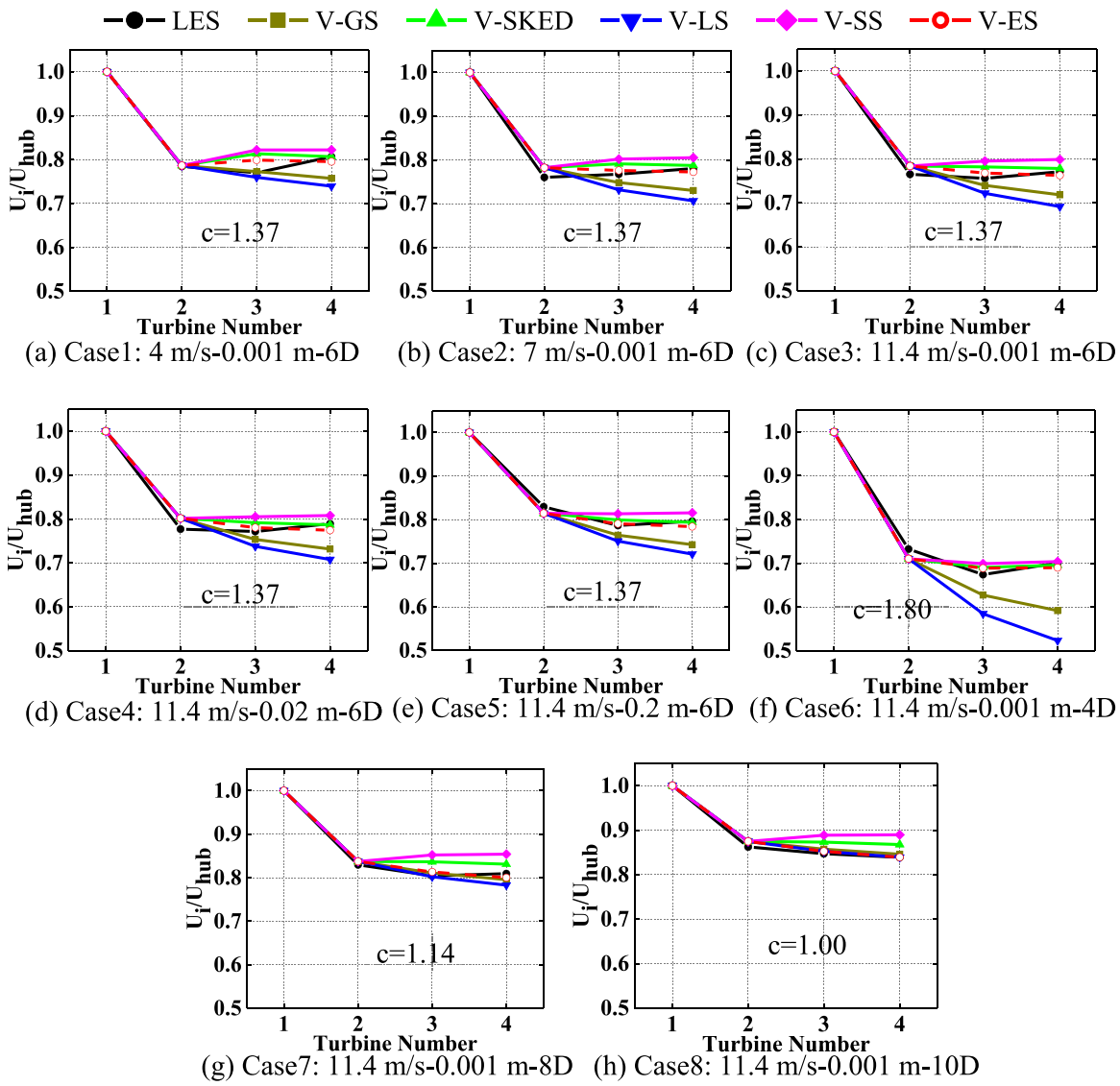

Fig. 19. Comparison of inflow velocities among wake velocity superposition models and numerical simulation.

Table 6
Average relative errors of inflow velocities of turbines 3–4 in different superposition models.

	V-GS	V-SKED	V-LS	V-SS	V-ES
Case 1	3.23%	2.83%	4.83%	4.34%	2.58%
Case 2	4.48%	1.99%	7.07%	3.85%	1.06%
Case 3	4.47%	2.19%	7.40%	4.40%	1.34%
Case 4	4.83%	1.52%	7.35%	3.35%	1.46%
Case 5	4.77%	1.03%	7.00%	2.92%	0.99%
Case 6	11.26%	1.87%	19.32%	2.08%	1.59%
Case 7	1.25%	3.35%	1.76%	5.76%	1.11%
Case 8	1.00%	3.25%	0.32%	5.47%	0.32%
Mean value	4.41%	2.25%	6.88%	4.02%	1.31%

4.2. Multi-turbine wake velocity superposition models

In this section, single turbine wake velocity model and different wake velocity superposition models (see Table 4) will be used to calculate the multi-turbine wake average velocity, where the inflow turbulence intensity of downstream turbines is obtained from numerical simulation results. In such a treatment, the accuracy of velocity superposition models can be studied without considering the error caused by turbulence intensity superposition models.

4.3. Multi-turbine turbulence intensity superposition models

If only the analytical models are used to calculate the multi-turbine wake velocity and turbulence intensity, the turbulence intensity superposition model is also required.

From the simulation results of the turbine wake turbulence intensity in Section 3.2, the turbulence intensity field is found to be similar to the wake velocity field. Both of them stabilize from turbine 2, and has a similar recovery trend. Inspired by this observation, the turbulence intensity superposition model can be constructed from the wake velocity superposition model, as in Table 5:

4.4. New wake superposition model

4.4.1. The exponential superposition model for velocity

Inspired by V-LS and V-SS, the power exponent can be made to become a varying constant, and the exponential superposition model for velocity (V-ES) is proposed:

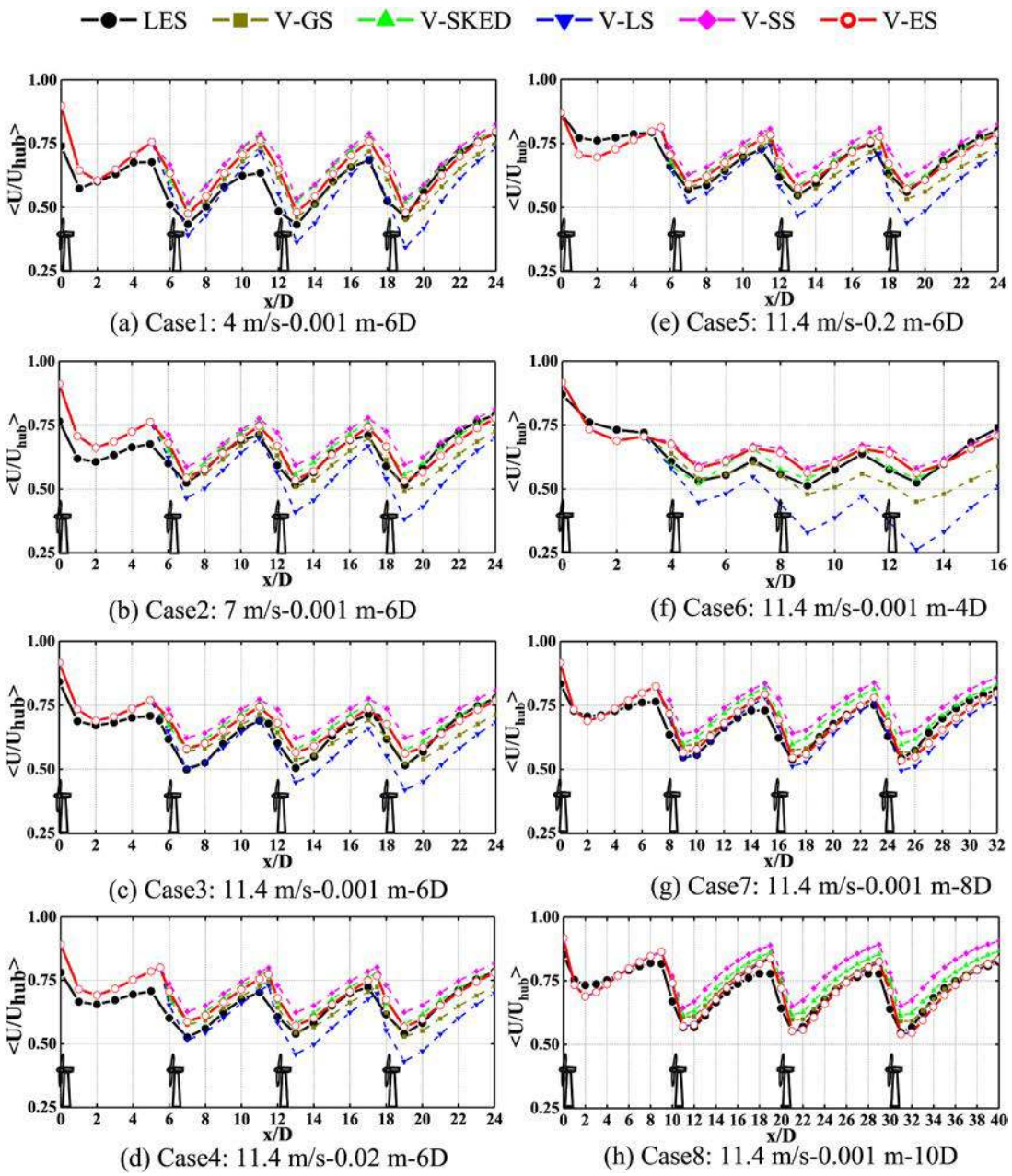

Fig. 20. Comparison of wake average velocities among velocity superposition models and numerical simulation in different downstream positions.

$$u_i = u_0\left(1-\left(\sum_{j=1}^{n}\left(1-\frac{u_{ij}}{u_j}\right)^{c}\right)^{\frac{1}{c}}\right) \tag{13}$$

where c is the model constant. With Case 3 (11.4 m/s −5.5%-6D) as an example (shown in Fig. 18), the accuracy of model results can be adjusted by changing c. When c is 1.40, the result of velocity exponential superposition is closest to the numerical simulation results.

In this way the best constant c for each case simulated in section 3 can be determined. Clearly, this constant only changes with the turbine spacing, as shown in Fig. 19. In the following discussion, the velocity geometric sum, velocity sum of kinetic energy deficit, velocity linear superposition and velocity sum of square are referred as to V-GS, V-SKED, V-LS and V-SS, respectively.

Based on the results of the other three spacing (4D, 8D, 10D) in numerical simulation, the model constant c under each spacing can be fitted into Eq. (14):

$$c = 4.579(\Delta x/D)^{-0.698} + 0.06462 \tag{14}$$

Table 6 summarizes the average value of the relative error of inflow velocity among models and numerical results for turbines 3–4, where the error is defined as:

$$E_U = \left(\left|\left(U_3^m - U_3^n\right)/U_3^n\right| + \left|\left(U_4^m - U_4^n\right)/U_4^n\right|\right)/2 \tag{15}$$

where U_i^m is the inflow velocity of turbine i from models, and U_i^n is the inflow velocity of turbine i from numerical simulation.

It can be seen that among the five models, the relative error of velocity exponential superposition is less than 2.58% in different conditions and it has the larger applicability.

Fig. 20 shows the average velocity (spatially averaged within the rotor diameter) on hub height plane at different downstream positions for the numerical simulation and different superposition models. Fig. 21 shows the relative errors of the different wake velocity superposition

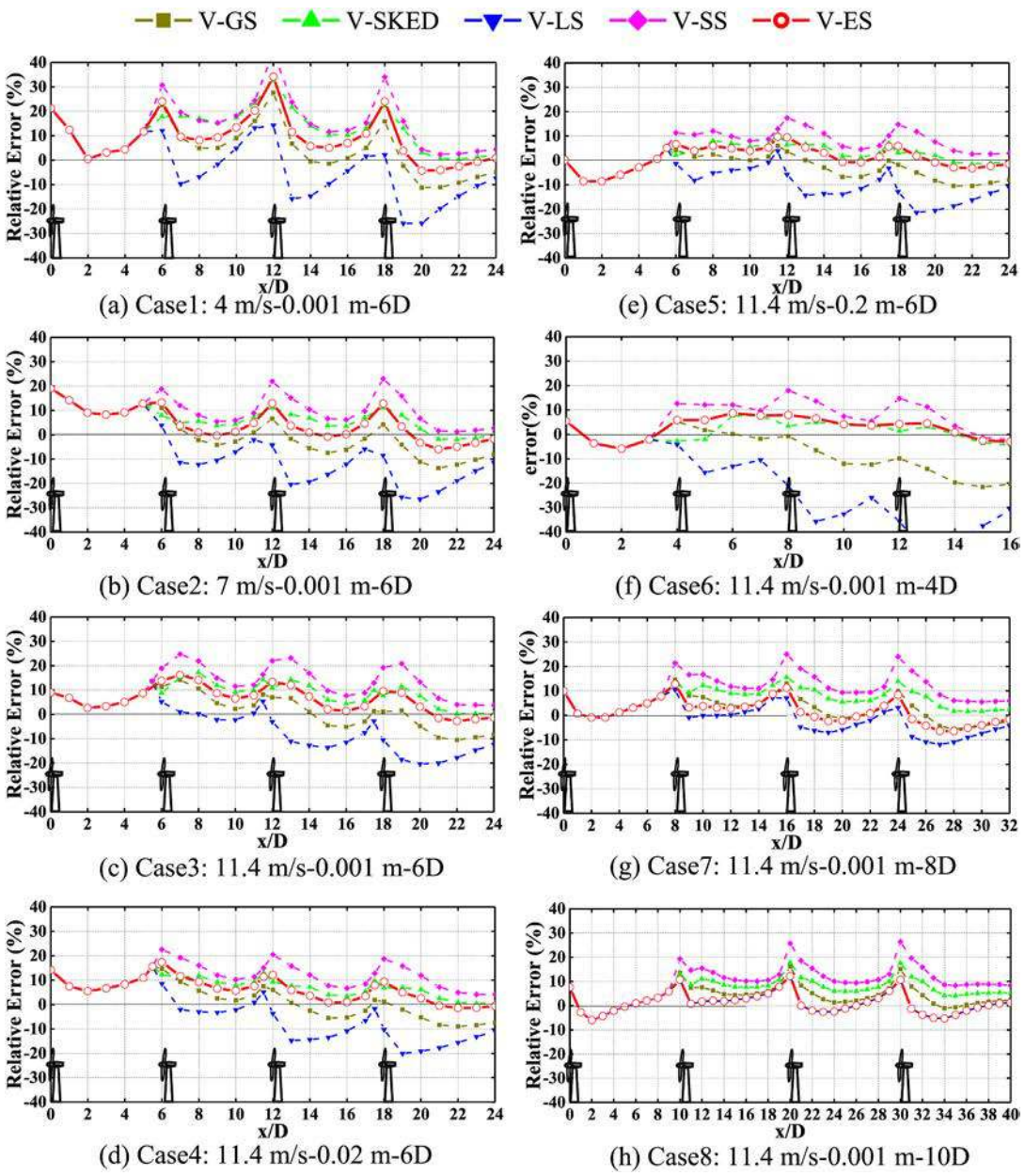

Fig. 21. Relative errors of wake average velocities among velocity superposition models and numerical simulation in different downstream positions.

models.

The influence of the inflow mean velocity, turbulence intensity and spacing on the accuracy of the turbine wake velocity superposition models is discussed respectively:

(1) Cases 1–3 under different inflow mean velocities. As shown in Figs. 20–21 (a)–(c), the accuracy of the different existing classic superposition models does not change obviously with the increase of inflow mean velocity. Velocity exponential superposition is the most accurate among the five velocity superposition models.

(2) Cases 3–5 under different inflow turbulence intensity. As shown in Figs. 20–21 (c)–(e), with the increase of inflow turbulence intensity, the accuracy of the different existing classic superposition models still does not change obviously. Velocity exponential superposition is relatively most accurate among the five velocity superposition models.

(3) Cases 3, 6–8 under different spacing. As shown in Figs. 20–21 (c) and (f)-(h), with the increase of spacing, the results of the different existing classic superposition models will become closer, and the overall error will decrease. Especially when the spacing is 10D, the relative error of all models in far wake region is less than 10%. This is due to the fact that the flow field is complex in small spacing, and the accuracy of different existing classic superposition models varies greatly. With the increase of the turbine spacing, the wake velocity of different superposition models will tend to be the inflow velocity. The accuracy of velocity linear superposition gradually increases, and the accuracy of velocity sum of squares gradually decreases with the increase of spacing. And the relative error of velocity exponential superposition remains smallest in different spacing.

In general, the decreasing order of the average wake velocity of different existing four classic superposition models in the magnitude is velocity sum of squares, velocity sum of kinetic energy deficit, velocity

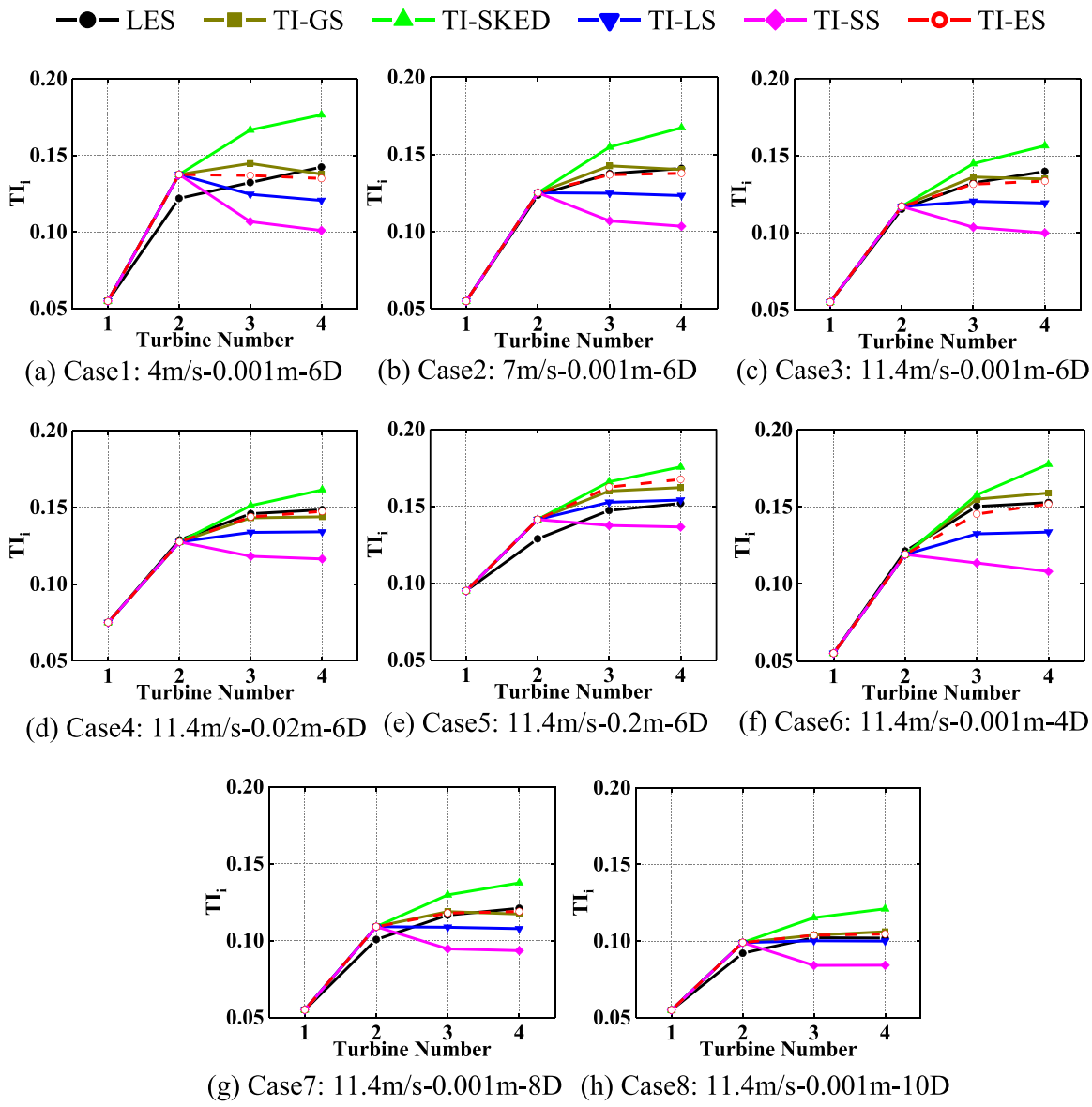

Fig. 22. Comparison of inflow turbulence intensities among superposition models and numerical simulation.

Table 7
Average absolute error of inflow turbulence intensities of turbines 3–4 of superposition models.

	TI-GS	TI-SKED	TI-LS	TI-SS	TI-ES
Case 1	0.83%	3.61%	1.75%	3.01%	0.46%
Case 2	0.29%	2.23%	1.67%	3.05%	0.14%
Case 3	0.42%	1.46%	1.71%	3.03%	0.26%
Case 4	0.36%	0.88%	1.36%	2.71%	0.13%
Case 5	1.13%	2.26%	0.42%	1.27%	1.42%
Case 6	0.54%	1.65%	1.92%	3.55%	0.22%
Case 7	0.30%	1.48%	1.14%	2.26%	0.13%
Case 8	0.29%	1.63%	0.23%	1.76%	0.17%
Mean value	0.52%	1.9%	1.28%	2.58%	0.37%

geometric sum and velocity linear superposition, and this trend is not affected by the change of the inflow mean velocity, turbulence intensity and spacing.

4.4.2. The exponential superposition model for turbulence intensity

The same idea can also be used for the turbulence intensity superposition and the corresponding turbulence intensity exponential superposition given as:

$$I_i = I_0\left(1+\left(\sum_{j=1}^{n}\left(\frac{I_{ij}}{I_j}-1\right)^{d}\right)^{\frac{1}{d}}\right) \tag{16}$$

where d is the model constant, and the optimal value of d is 0.8 as shown in Fig. 22. In the following discussion, the turbulence intensity geometric sum, turbulence intensity sum of kinetic energy deficit, turbulence intensity linear superposition and turbulence intensity sum of square are referred as to TI-GS, TI-SKED, TI-LS and TI-SS, respectively.

Table 7 summarizes the average value of the absolute error of inflow turbulence intensity among models and numerical results of turbines 3–4, where the error is defined as:

$$E_{TI} = \left(\left|TI_3^m - TI_3^n\right| + \left|TI_4^m - TI_4^n\right|\right)/2 \tag{17}$$

where TI_i^m is the inflow turbulence intensity of turbine i from models and TI_i^n is the inflow turbulence intensity of turbine i from numerical simulation.

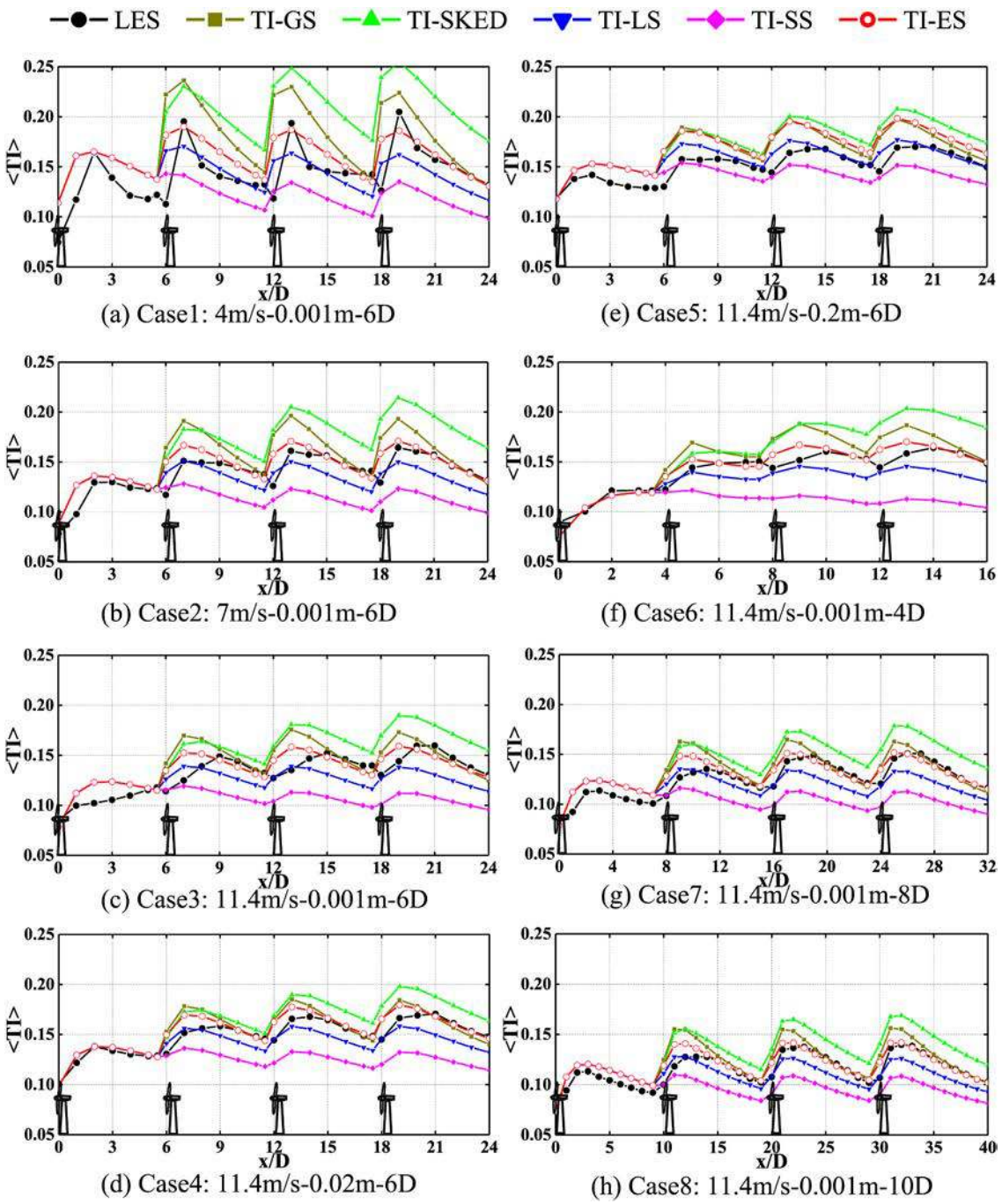

Fig. 23. Comparison of wake turbulence intensities among superposition models and numerical simulation in different downstream positions.

It can be seen that among the five models, the absolute error of the turbulence intensity exponential superposition is less than 1% in different conditions, with the relatively highest applicability. Therefore, turbulence intensity exponential superposition can satisfactorily predict the turbulence intensity of multi-turbine wakes.

Fig. 23 shows the average turbulence intensity (spatially averaged within the rotor diameter) on hub height plane at different downstream positions. It can be seen although the accuracy of turbulence intensity exponential superposition differs little from that of turbulence intensity geometric sum in the far wake region, turbulence intensity exponential superposition is significantly better than turbulence intensity geometric sum in the near wake region.

5. Validation in real wind farm

In order to further validate the accuracy and applicability of exponential superposition (ES) for wake velocity and turbulence intensity, the data of Lillgrund offshore wind farm and Horns Rev wind farm are used.

5.1. *Lillgrund offshore wind farm*

The Lillgrund offshore wind farm is located in the ØResund, between Sweden and Denmark, 6–8 km off the west coast of Sweden. The wind farm includes 48 SWT-2.3-93 turbines (Rotor diameter is 93 m and hub height is 65 m) with a total installed capacity of 110 MW. Turbines in this wind farm are approximately aligned in lines, and the spacing is

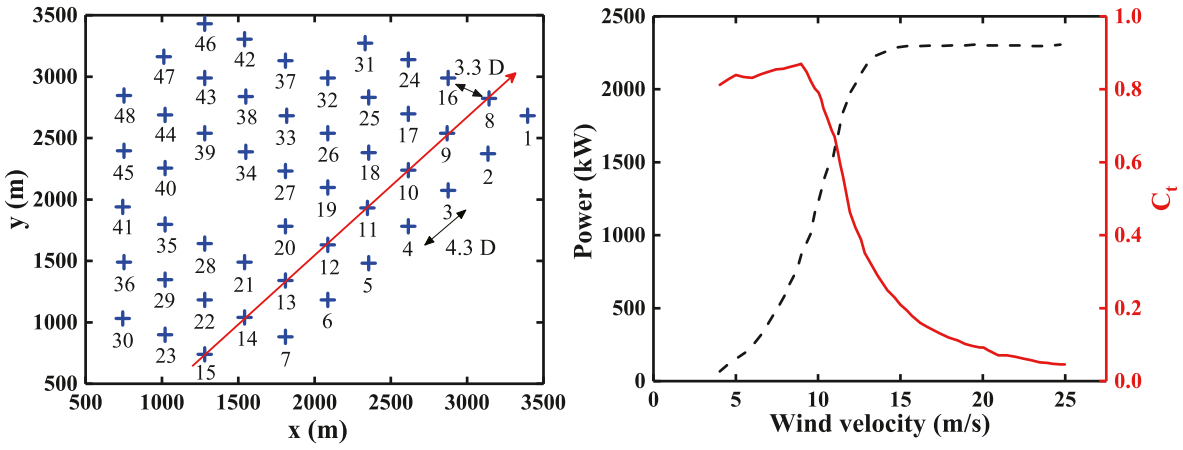

(a) Layout of Lillgrund offshore wind farm

(b) Thrust coefficient and power curves of SWT-2.3-93

Fig. 24. Basic information of Lillgrund offshore wind farm (Churchfield et al., 2012b; Göçmen and Giebel, 2016).

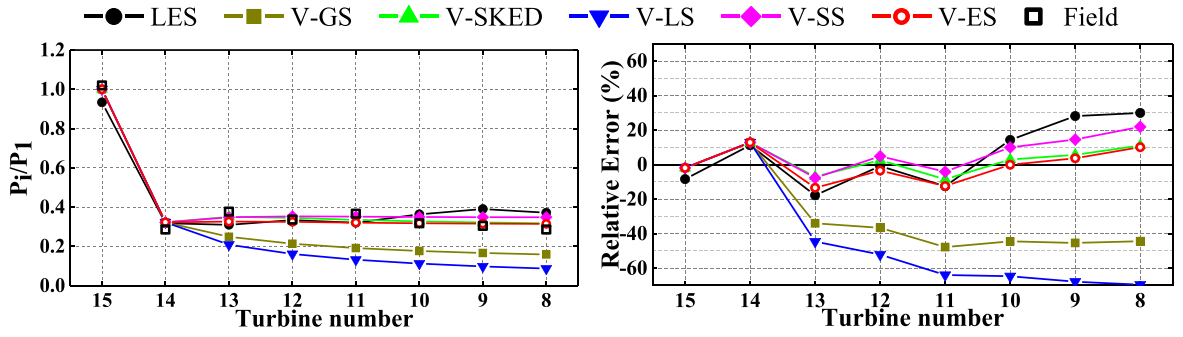

(a) Power of each turbine

(b) Relative error of different methods

Fig. 25. Comparison of powers of turbines on Column B among field data, LES and different methods.

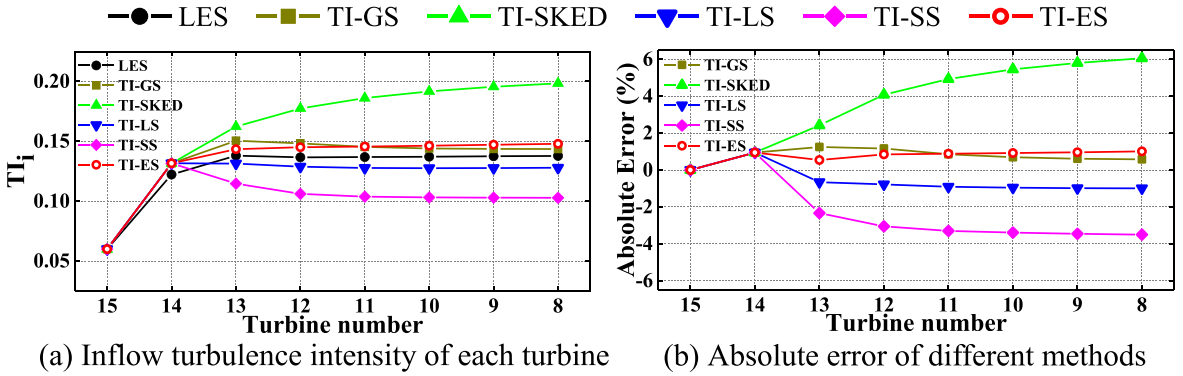

(a) Inflow turbulence intensity of each turbine

(b) Absolute error of different methods

Fig. 26. Comparison of inflow turbulence intensities of turbines on Column B among LES and different methods.

small, with spacing of $4.3D \times 3.3D$ as shown in Fig. 24 (a). The thrust coefficient and power curves of SWT-2.3-93 are shown in Fig. 24 (b).

Column B in the Lillgrund wind farm is chosen for the verification, which contains 8 turbines with a spacing of 4.3D and is similar to Case 6 simulated in Section 3.2.2. According to the literature (Bergström, 2009), the direction of the southwest 221.6° for the field data is selected, because in this case the inflow wind is just the same as the direction of Column B. The inflow mean velocity of 9 m/s is chosen on the hub height, since the thrust coefficient is the largest and can produce the strongest wake effect, and the inflow turbulence intensity is about 6% in this wind direction, which is the same with the inflow condition of field data (Dahlberg, 2009) and LES simulation (Churchfield et al., 2012b).

The comparisons among the superposition models, the field data (Dahlberg, 2009) and LES results (Churchfield et al., 2012b) are shown in Figs. 25–26. In Fig. 25, the results of the four existing velocity superposition models and velocity exponential superposition proposed in this paper are compared with the field data and the LES results. It can be seen that velocity exponential superposition has higher accuracy

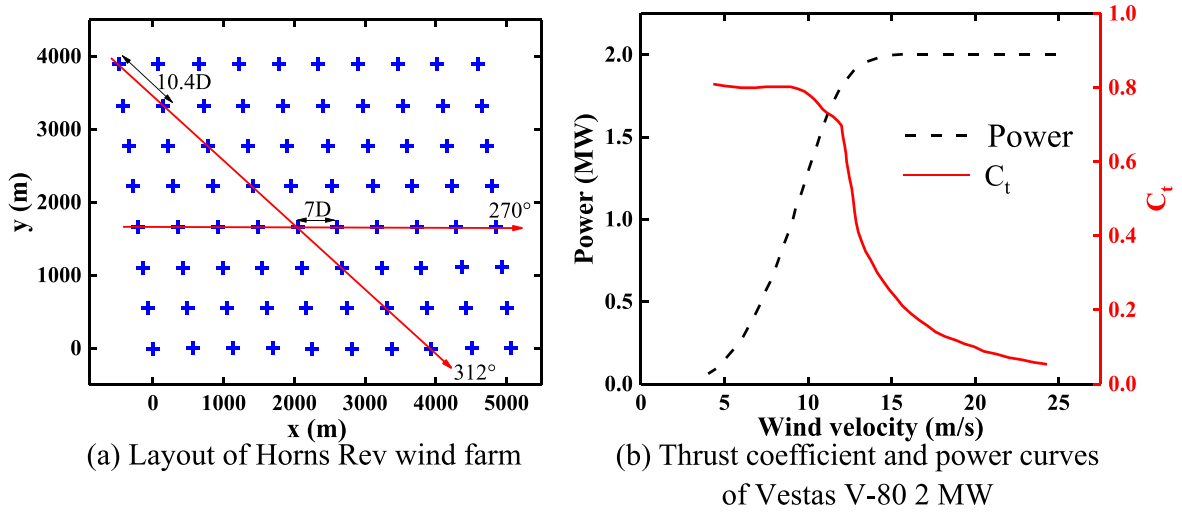

Fig. 27. Basic information of Horns Rev wind farm (Porté-Agel et al., 2013).

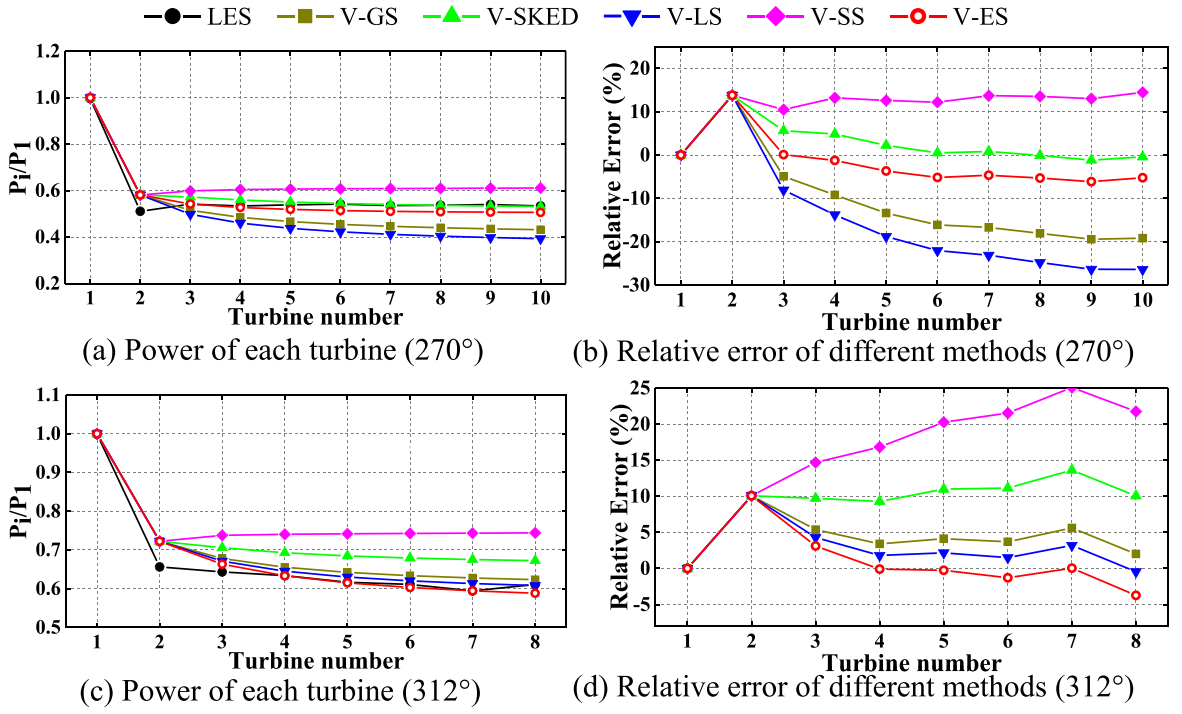

Fig. 28. Comparison of powers of turbines on wind directions of 270° and 312° among LES and different methods.

compared with other models. In Fig. 26, the results of different turbulence intensity superposition models are compared with the LES results. It can be seen that the maximum absolute error of the turbulence intensity exponential superposition (TI-ES) is less than 1%, which also proves the accuracy and applicability of this model.

5.2. *Horns Rev wind farm*

The Horns Rev wind farm is located in the eastern North Sea, around 15 km off the westernmost point of Denmark. The wind farm includes 80 Vestas V-80 2 MW wind turbines (Rotor diameter is 80 m and hub height is 70 m). The wind turbines are distributed along two directions, the East-West direction and approximately 7° North by South as shown in Fig. 27 (a). The thrust coefficient and power curves of Vestas V-80 2 MW are shown in Fig. 27 (b).

Wind directions of 270° and 312° are chosen for the verification, which contains 10 and 8 turbines with spacings of 7*D* and 10.4*D*. According to the literature (Niayifar and Porté-Agel, 2016) (Porté-Agel et al., 2013), the inflow mean velocity is 8 m/s on the hub height, and the inflow turbulence intensity is about 7.7%.

The comparisons among the superposition models and the LES results (Niayifar and Porté-Agel, 2016) (Porté-Agel et al., 2013) are shown in Figs. 28–29. In Fig. 28, the results of the four existing velocity superposition models and velocity exponential superposition proposed in this paper are compared with the LES results in aforementioned two inflow wind directions. It can be seen that in Fig. 28 (a)–(b) when the turbine spacing is 7*D*, velocity exponential superposition and velocity sum of kinetic energy deficit have similar results in power prediction and velocity sum of kinetic energy deficit is slightly more accurate than velocity exponential superposition. However, in Fig. 28 (c)–(d), when

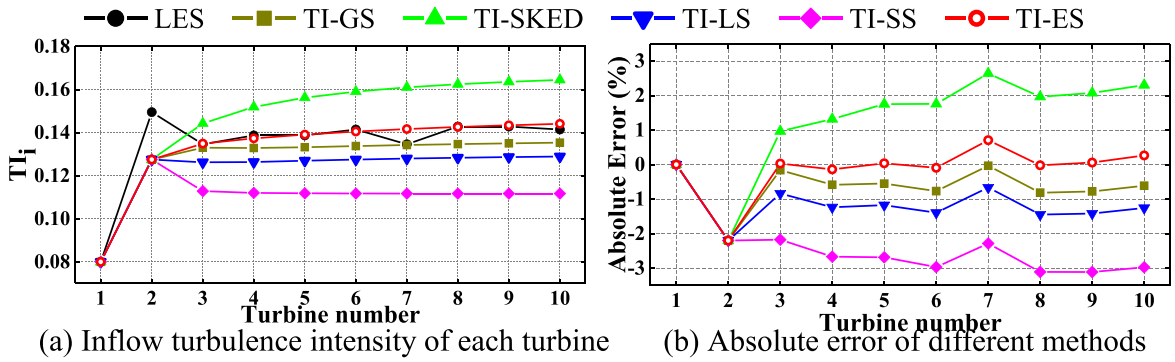

(a) Inflow turbulence intensity of each turbine (b) Absolute error of different methods

Fig. 29. Comparison of inflow turbulence intensities of turbines on wind directions of 270° among LES and different methods.

the turbine spacing is 10.4*D*, velocity exponential superposition is much more accurate than velocity sum of kinetic energy deficit and it has the highest accuracy. In Fig. 29, the results of different turbulence intensity superposition models are compared with the LES results. It can be seen that the averaged absolute error of turbines 3–10 of the turbulence intensity exponential superposition is 0.138%, and that of the turbulence intensity geometric sum is 0.534%. This also proves the accuracy and applicability of the newly proposed model.

6. Conclusions

In this study, LES and ALM are used to simulate and analyze the aligned multi-turbine wake under the influence of various factors, and the superposition models of wake average velocity and turbulence intensity are studied systematically. The observations and conclusions are given as follows:

(1) The influence of different inflow mean velocities, turbulence intensities and spacing on multi-turbine wake is analyzed, and it can be found that:
(a) When the inflow mean velocity varies at and below rated velocity with inflow turbulence intensity of 5.5% and spacing of 6D, the wake of the downstream turbines is becoming stable from turbine 2.
(b) When the inflow turbulence intensity varies between 5.5% and 9.5% with inflow mean velocity of 11.4 m/s and spacing of 6D, it mainly affects the wake recovery speed of turbine 1, but has little influence on the wake of other downstream turbines.
(c) When the spacing varies between 4D and 10D with inflow mean velocity of 11.4 m/s and turbulence intensity of 5.5%, the wake of the downstream turbines is becoming stable from turbine 2 too. The larger the spacing is, the more similar the wake of downstream turbines will be.

(2) The existing four velocity superposition models is evaluated based on the numerical simulation results, and it can be found that: When the inflow mean velocity is smaller than the rated velocity, the mean velocity and turbulence intensity of the inflow have less influence on the accuracy of the existing four velocity superposition models compared with the spacing. The smaller the spacing is, the higher the accuracy of velocity sum of squares is, while the larger the spacing is, the higher the accuracy of velocity linear superposition is. Besides, the decreasing order of the magnitude for the results of the existing four velocity superposition models is velocity sum of squares, velocity sum of kinetic energy deficit, velocity geometric sum and velocity linear superposition.

(3) Exponential superposition is proposed for the wake velocity and turbulence intensity. Exponential superposition is more accurate compared with the existing four velocity superposition models.

(4) Exponential superposition for velocity and turbulence intensity is evaluated by the benchmark data from Lillgrund wind farm and Horns Rev wind farm. It is shown that exponential superposition behaves well in the real wind farms.

CRediT authorship contribution statement

Runze Zhang: Methodology, Validation, Writing – original draft. **Zhiqiang Xin:** Writing – review & editing. **Guoqing Huang:** Conceptualization, Supervision, Writing – review & editing. **Bowen Yan:** Review, Formal analysis. **Xuhong Zhou:** Formal analysis. **Xiaowei Deng:** Formal analysis.

Declaration of competing interest

The authors declare that they have no known competing financial interests or personal relationships that could have appeared to influence the work reported in this paper.

Data availability

No data was used for the research described in the article.

Acknowledgments

The supports by the National Natural Science Foundation of China (Grant No. 52178456), 111 Project (Grant No. B18062), Science and Technology R & D Project of Shandong Academy of Sciences (Contract Nos. 2020QN007; 2020QN008; 2019NO.2; 2020KJC-GH04; 2020GXRC045) are greatly acknowledged.

References

Barthelmie, R.J., Hansen, K., Frandsen, S.T., Rathmann, O., Schepers, J.G., Schlez, W., Philips, J., Rados, K., Zervos, A., Politis, E.S., Chaviaropoulos, P.K., 2009. Modelling and measuring flow and wind turbine wakes in large wind farms offshore. Wind Energy 12, 431–444.
Bastankhah, M., Porté-Agel, F., 2014. A new analytical model for wind-turbine wakes. Renew. Energy 70, 116–123.
Bergström, H., 2009. Meteorological Conditions at Lillgrund.
Breton, S.P., Shen, W.Z., Ivanell, S., 2017. Validation of the actuator disc and actuator line techniques for yawed rotor flows using the New Mexico experimental data. J. Phys. Conf. 854, 012005.
Brugger, P., Debnath, M., Scholbrock, A., Fleming, P., Moriarty, P., Simley, E., Jager, D., Roadman, J., Murphy, M., Zong, H., Porté-Agel, F., 2020. Lidar measurements of yawed wind turbine wakes: characterisation and validation of analytical models. Wind Energy Sci. 5 (4), 1253–1272.
Churchfield, M.J., Lee, S., Michalakes, J., Moriarty, P.J., 2012a. A numerical study of the effects of atmospheric and wake turbulence on wind turbine dynamics. J. Turbul. 13, N14.
Churchfield, M.J., Lee, S., Moriarty, P., Martinez, L., Leonardi, S., Vijayakumar, G., Brasseur, J., 2012b. A Large-Eddy Simulation of Wind-Plant Aerodynamics, 50th AIAA Aerospace Sciences Meeting Including the New Horizons Forum and Aerospace Exposition, p. 537.

Crespo, A., Herna, J., 1996. Turbulence characteristics in wind-turbine wakes. J. Wind Eng. Ind. Aerod. 61 (1), 71–85.
Dahlberg, J.Å., 2009. Assessment of the Lillgrund Wind Farm: Power Performance Wake Effects.
de Villiers, E., 2006. The Potential of Large Eddy Simulation for the Modeling of Wall-Bounded Flows. PhD Thesis. Department of Mechanical Engineering, Imperial College of Science, Technology, and Medicine, London.
Draper, M., Guggeri, A., Mendina, M., et al., 2018. A large eddy simulation-actuator line model framework to simulate a scaled wind energy facility and its application. J. Wind Eng. Ind. Aerod. 182, 146–159.
Espana, G., Aubrun, S., Loyer, S., et al., 2012. Wind tunnel study of the wake meandering downstream of a modelled wind turbine as an effect of large scale turbulent eddies. J. Wind Eng. Ind. Aerod. 101, 24–33.
Etling, D., 1996. Modelling the Vertical Abl Structure. Modelling Of Atmospheric Flow Fields, p. 45.
Gaumond, M., Réthoré, P.E., Ott, S., Pena, A., Bechmann, A., Hansen, K.S., 2014. Evaluation of the wind direction uncertainty and its impact on wake modeling at the Horns Rev offshore wind farm. Wind Energy 17 (8), 1169–1178.
Glauert, H., 1926. The Analysis of Experimental Results in the Windmill Brake and Vortex Ring States of an Airscrew. HM Stationery Office.
Glauert, H., 1935. Airplane Propellers, Aerodynamic Theory. Springer, Berlin, Heidelberg.
Göçmen, T., Giebel, G., 2016. Estimation of turbulence intensity using rotor effective wind speed in Lillgrund and Horns Rev-I offshore wind farms. Renew. Energy 99, 524–532.
Hassan, U., Hassan, G., 1993. A Wind Tunnel Investigation of the Wake Structure within Small Wind Turbine Farms. Harwell Laboratory, Energy Technology Support Unit: Brighton, UK.
Ishihara, T., Qian, G.W., 2018. A new Gaussian-based analytical wake model for wind turbines considering ambient turbulence intensities and thrust coefficient effects. J. Wind Eng. Ind. Aerod. 177, 275–292.
Ishihara, T., Yamaguchi, A., Fujino, Y., 2004. Development of a new wake model based on a wind tunnel experiment. Global Wind Power 6.
Jensen, N.O., 1983. A Note on Wind Generator Interaction, pp. 30–43.
Jha, P.K., Churchfield, M.J., Moriarty, P.J., et al., 2014. Guidelines for volume force distributions within actuator line modeling of wind turbines on large-eddy simulation-type grids. J. Sol. Energy Eng. 136 (3).
Jonkman, J., Buhl Jr., M., 2005. FAST User's Guide, Rep. NREL/TP-500-38230. National Renewable Energy Laboratory, Colorado.
Jonkman, J.M., Butterfield, S., Musial, W., Scott, G., 2009. Definition of a 5MW Reference Wind Turbine for Offshore System Development. office of scientific & technical information technical reports.
Kalvig, S., Manger, E., Hjertager, B., 2014. Comparing different CFD wind turbine modelling approaches with wind tunnel measurements. J. Phys. Conf. 555 (1), 012056.
Katic, I., Højstrup, J., Jensen, N.O., 1986a. A simple model for cluster efficiency. Eur. Wind Energy Assoc. Conf. Exhibit. 1, 407–410.
Katic, I., Højstrup, J., Jensen, N.O., 1986b. A Simple Model for Cluster Efficiency, vol. 86. EWEC, Rome, Italy, pp. 406–410.
Kim, H., Kim, K., Bottasso, C.L., et al., 2018. Wind turbine wake characterization for improvement of the Ainslie eddy viscosity wake model. Energies 11 (10), 2823.
Krogstad, P.Å., Eriksen, P.E., 2013. Blind test" calculations of the performance and wake development for a model wind turbine. Renew. Energy 50, 325–333.
Krogstad, P.Å., Sætran, L., Adaramola, M.S., 2015. Blind Test 3" calculations of the performance and wake development behind two in-line and offset model wind turbines. J. Fluid Struct. 52, 65–80.
Kuo, J.Y.J., Romero, D.A., Amon, C.H., 2014. A Novel Wake Interaction Model for Wind Farm Layout Optimization, ASME 2014 International Mechanical Engineering Congress and Exposition. American Society of Mechanical Engineers Digital Collection.
Lissaman, P.B.S., 1979. Energy effectiveness of arbitrary arrays of wind turbines. J. Energy 3 (6), 323–328.
Lopes, A.M.G., Vicente, A.H.S.N., Sánchez, O.H., et al., 2022. Operation assessment of analytical wind turbine wake models. J. Wind Eng. Ind. Aerod. 220, 104840.
Martinez, L., Leonardi, S., Churchfield, M.J., Moriarty, P.A., 2012. A Comparison of Actuator Disk and Actuator Line Wind Turbine Models and Best Practices for Their Use, 50th AIAA Aerospace Sciences Meeting Including the New Horizons Forum and Aerospace Exposition, p. 900.
Martínez-Tossas, L.A., Churchfield, M.J., Leonardi, S., 2015a. Large eddy simulations of the flow past wind turbines: actuator line and disk modeling. Wind Energy 18 (6), 1047–1060.
Martínez-Tossas, L.A., Churchfield, M.J., Leonardi, S., 2015b. Large eddy simulations of the flow past wind turbines: actuator line and disk modeling. Wind Energy 18 (6), 1047–1060.
Masters, G.M., 2013. Renewable and Efficient Electric Power Systems. John Wiley & Sons.
Mehta, D., Van Zuijlen, A.H., Koren, B., et al., 2014. Large Eddy Simulation of wind farm aerodynamics: a review. J. Wind Eng. Ind. Aerod. 133, 1–17.
Mo, J.O., Choudhry, A., Arjomandi, M., et al., 2013a. Effects of wind speed changes on wake instability of a wind turbine in a virtual wind tunnel using large eddy simulation. J. Wind Eng. Ind. Aerod. 117, 38–56.
Mo, J.O., Choudhry, A., Arjomandi, M., et al., 2013b. Large eddy simulation of the wind turbine wake characteristics in the numerical wind tunnel model. J. Wind Eng. Ind. Aerod. 112, 11–24.
Moeng, C.H., 1984. A large-eddy-simulation model for the study of planetary boundary-layer turbulence. J. Atmos. Sci. 41 (13), 2052–2062.
Niayifar, A., Porté-Agel, F., 2016. Analytical modeling of wind farms: a new approach for power prediction. Energies 9 (9), 741.
Nygaard, N.G., Jensen, L., Downey, R., et al., 2013. Construction and validation of a new offshore wake model. In: Proceedings of the International Conference on Aerodynamics of Offshore Wind Energy Systems and Wakes (ICOWES) Conference, p. 1719. Lyngby, Danmark.
Pierella, F., Krogstad, P.Å., Sætran, L., 2014. Blind Test 2 calculations for two in-line model wind turbines where the downstream turbine operates at various rotational speeds. Renew. Energy 70, 62–77.
Pique, A., Miller, M.A., Hultmark, M., 2020. Characterization of the wake behind a horizontal-axis wind turbine (HAWT) at very high Reynolds numbers. In: Journal of Physics: Conference Series, vol. 1618. IOP Publishing, 062039, 6.
Porté-Agel, F., Lu, H., Wu, Y.T., 2010. A large-eddy simulation framework for wind energy applications. In: The Fifth International Symposium on Computational Wind Engineering, vol. 23. Chapel Hill, p. 27.
Porté-Agel, F., Wu, Y.T., Lu, H., Conzemius, R.J., 2011. Large-eddy simulation of atmospheric boundary layer flow through wind turbines and wind farms. J. Wind Eng. Ind. Aerod. 99 (4), 154–168.
Porté-Agel, F., Wu, Y.T., Chen, C.H., 2013. A numerical study of the effects of wind direction on turbine wakes and power losses in a large wind farm. Energies 6 (10), 5297–5313.
Porté-Agel, F., Bastankhah, M., Shamsoddin, S., 2020. Wind-turbine and wind-farm flows: a review. Boundary-Layer Meteorol. 174 (1), 1–59.
Qian, G.W., Ishihara, T., 2021. Wind farm power maximization through wake steering with a new multiple wake model for prediction of turbulence intensity. Energy 220, 119680.
Quarton, D.C., Ainslie, J.F., 1990. Turbulence in Wind Turbine Wakes. Wind Engineering, pp. 15–23.
Sanderse, B., 2009. Aerodynamics of Wind Turbine Wakes Literature Review. ECN, Nethrlands. Technical Report ECN-E-09-016.
Sawyer, S., Qiao, L., Fried, L., 2018. GLOBAL WIND REPORT - Annual Market Update 2017.
Schumann, U., 1975. Subgrid scale model for finite difference simulations of turbulent flows in plane channels and annuli. J. Comput. Phys. 18 (4), 376–404.
Shao, Z., Wu, Y., Li, L., Han, S., Liu, Y., 2019. Multiple wind turbine wakes modeling considering the faster wake recovery in overlapped wakes. Energies 12 (4), 680.
Simisiroglou, N., Polatidis, H., Ivanell, S., 2018. Wind Farm Power Production Assessment: a Comparative Analysis of Two Actuator Disc Methods and Two Analytical Wake Models. Wind Energy Science Discussions, pp. 1–13.
Smagorinsky, J., 1963. General circulation experiments with the primitive equations: I. The basic experiment. Mon. Weather Rev. 91 (3), 99–164.
Sørensen, N.N., 2009. CFD modelling of laminar-turbulent transition for airfoils and rotors using the $\gamma-$ model. Wind Energy: Int. J. Prog. Appl. wind Power Convers. Technol. 12 (8), 715–733.
Sorensen, J.N., Shen, W.Z., 2002. Numerical modeling of wind turbine wakes. J. Fluid Eng. 124 (2), 393–399.
Stull, R.B., 1988. An Introduction to Boundary Layer Meteorology. Springer Netherlands.
Sun, H., Gao, X., Yang, H., 2020. A review of full-scale wind-field measurements of the wind-turbine wake effect and a measurement of the wake-interaction effect. Renew. Sustain. Energy Rev. 132, 110042.
Tang, H., Lam, K.M., Shum, K.M., Li, Y., 2019. Wake effect of a horizontal axis wind turbine on the performance of a downstream turbine. Energies 12 (12), 2395.
Thomsen, K., Sørensen, P., 1999. Fatigue loads for wind turbines operating in wakes. J. Wind Eng. Ind. Aerod. 80, 121–136.
Ti, Z., Deng, X.W., Yang, H., 2020. Wake modeling of wind turbines using machine learning. Appl. Energy 257, 114025.
Tian, L., Zhu, W., Shen, W., et al., 2015. Development and validation of a new two-dimensional wake model for wind turbine wakes. J. Wind Eng. Ind. Aerod. 137, 90–99.
Tian, L., Zhu, W., Shen, W., et al., 2017. Prediction of multi-wake problems using an improved Jensen wake model. Renew. Energy 102, 457–469.
Troldborg, N., 2008. Actuator Line Modeling of Wind Turbine Wakes. PhD Thesis. Technical University of Denmark, Lyngby, Denmark.
Voutsinas, S., Rados, K., Zervos, A., 1990. On the Analysis of Wake Effects in Wind Parks. Wind Engineering, pp. 204–219.
Witha, B., Steinfeld, G., Dörenkämper, M., Heinemann, D., 2014. Large-eddy simulation of multiple wakes in offshore wind farms. J. Phys.: Conf. Series 555 (1), 012108.
Wu, Y.T., Porté-Agel, F., 2011. Large-eddy simulation of wind-turbine wakes: evaluation of turbine parametrisations. Boundary-Layer Meteorol. 138 (3), 345–366.
Wu, Y.T., Porté-Agel, F., 2012. Atmospheric turbulence effects on wind-turbine wakes: an LES study. Energies 5 (12), 5340–5362.
Wu, Y.T., Porté-Agel, F., 2015. Modeling turbine wakes and power losses within a wind farm using LES: an application to the Horns Rev offshore wind farm. Renew. Energy 75, 945–955.
Zhang, W., Markfort, C.D., Porté-Agel, F., 2013. Wind-turbine wakes in a convective boundary layer: a wind-tunnel study. Boundary-Layer Meteorol. 146 (2), 161–179.
Zong, H., Porté-Agel, F., 2020. A momentum-conserving wake superposition method for wind farm power prediction. J. Fluid Mech. 889.